OPTICAL CHARACTERIZATION OF THE DEAP-3600 DARK MATTER DETECTOR

by

Oleksandr Litvinov

A THESIS SUBMITTED IN PARTIAL FULFILLMENT OF

THE REQUIREMENTS FOR THE DEGREE OF

MASTER OF SCIENCE

in

The Faculty of Graduate and Postdoctoral Studies

(Physics)

THE UNIVERSITY OF BRITISH COLUMBIA

(Vancouver)

August 2019

The following individuals certify that they have read, and recommend to the Faculty of Graduate and Postdoctoral Studies for acceptance, the thesis entitled:

Optical characterization of the DEAP-3600 dark matter experiment

submitted by **Oleksandr Litvinov** in partial fulfillment of the requirements for the degree of **Master of Science** in **Physics**.

Examining Committee:

Fabrice Retiere, Physical Sciences Division, TRIUMF

Supervisor

Gordon Walter Semenoff, Physics

Supervisory committee member

Abstract

DEAP-3600 (Dark Matter Experiment using Argon for Pulse shape discrimination) is a dark matter experiment using liquid argon as a target to detect dark matter's Weakly Interacting Massive Particles (WIMPs). This work is a contribution to the experiment, focused on optical processes inside the inner detector. In order to re-scale and calibrate complex optical system used in the apparatus, the distribution of external light is studied. This work includes a qualitative description of the optical model, data analysis of light reflection from liquid/gas argon boundary and an attempt of estimating the refractive index of wave-shifter material.

Lay Summary

Very little is known about Dark Matter, despite the fact it comprises roughly 26% of the total energy of the Universe. DEAP-3600 (Dark Matter Experiment using Argon for Pulse shape discrimination) is a dark matter experiment focused on the direct detection of WIMPs (Weakly Interacting Massive Particles). It is designed to detect the scintillation light, emitted in clod liquid argon after interacting with WIMPs. Therefore, precise optical characterization of the apparatus is crucial for accurate particle detection. This work is a contribution to the optical part of the experiment, focused on its calibration methods.

Preface

This work is based on the apparatus and data of the DEAP-3600 experiment, the subject of a large international collaboration. The data analysis in chapter 3 is completed by author, O.Litvinov under supervision of F.Retiere and P.Giampa.

Table of Contents

List of Tables

List of Figures

Acknowledgments

First and foremost, my sincere gratitude goes to my supervisor, Fabrice Retiere, who made me a part of the DEAP collaboration, where I met so many incredible people. Thank you for all your help, support and opportunities you gave me over the last two years.

I owe special thanks to Pietro Giampa for sharing his experience, knowledge and wisdom. My progress would be barely possible without his leadership. Thank you, Pietro.

Thank you everyone in the DEAP collaboration. I learned a lot from each of you and I am happy I had the opportunity to get to know you better during our travels. Especial thanks go to Joe McLaughlin, who gave me a ride on my very first day with DEAP in Sudbury and became my good friend during his stay in Vancouver.

Apart from that, I owe a debt of gratitude to everyone who did not let me feel lonely throughout my workdays at TRIUMF. I am also grateful to all my university friends who made my studying and life enjoyable and fun.

Lastly, I would like to thank my family for all their love, patience and care. Thank you.

Chapter 1

Introduction

The nature and composition of Dark Matter remains one of the most pressing open-questions in modern physics. Growing interest in this topic can be easily explained with the fact that only 5% of the total mass-energy of the universe consists of baryonic matter. The remaining 95% are predicted to be a mixture of dark matter and dark energy with the portions of 26% and 69% correspondingly. Despite growing effort in experimental physics during the past few decades no direct observations have been made yet, although astrophysics provides multiple indirect evidences. Successful discovery of the dark matter may be the next major step in modern physics and a considerable expansion of the Standard Model.

1.1 Evidence For Dark Matter

Very little is known about Dark Matter except that it makes up for the vast majority of the mass of the universe and it does not interact with light. The first indirect evidence for the existence of Dark Matter came at the beginning of the 20th century. Even though we can not see it, we do know it is there due to gravitational anomalies which astrophysicists could observe at large scales. Astronomical observations reported more gravitational oddities, which could not be described without introducing the new concept of matter. Gravitational lensing and Cosmic Microwave Background stand out among others as essential indirect evidences for the existence

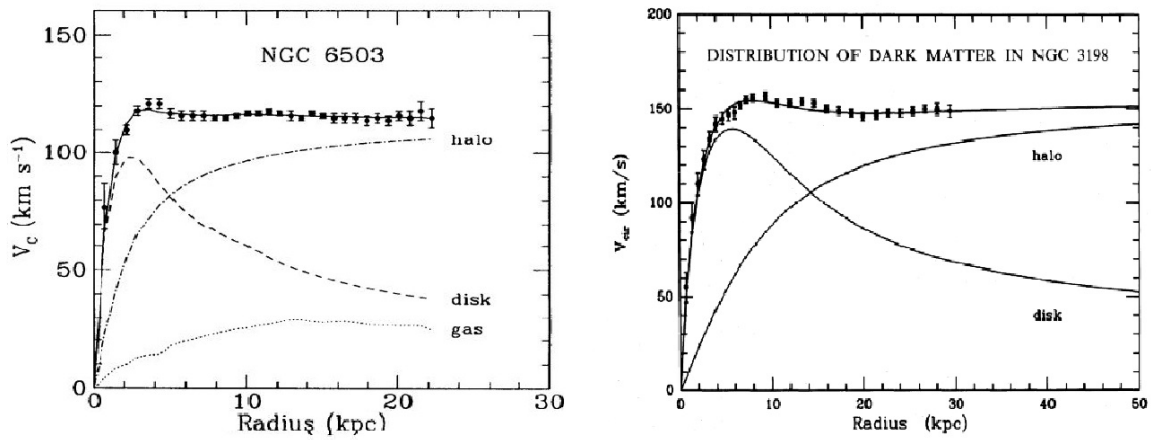

Figure 1.1: Observed galactic rotation curves of NGC 6503 (left) and NGC 3198 (right) as functions of the distance to the center of mass, and modelled portion of the disk, gas and halo structure [11, 41]

of Dark Matter.

1.1.1 Gravitational Anomalies

Fritz Zwicky first coined the term Dark Matter while studying the Coma cluster [17]. By calculating the velocity dispersion of the cluster, using Doppler shifts in its visible spectrum in 1933, Zwicky used the virial theorem (Eq. 1.1) to estimate the gravitational potential of the cluster:

$$< T >= -\frac{1}{2} < V > \tag{1.1}$$

where <T> is the mean kinetic energy in the center of mass frame and <V> is the mean potential energy of the system. Zwicky's calculations showed that the actual mass of the cluster was much higher than any predicted one based on the total masses of individual objects (estimated using luminosity measurements). He assumed that the bulk of the cluster must be filled with some new sort of matter which energy is dominated over the energy of visible cosmic objects.

The second indirect evidence of Dark Matter came from Vera Rubin in the early 1970s,

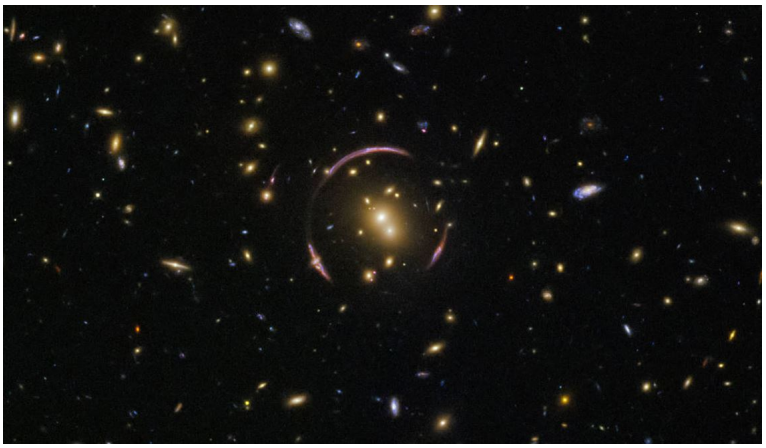

Figure 1.2: Observation of the lensing effect in space [29]

when she applied studying the rotational curve of the Andromeda galaxy. On the example of Andromeda Galaxy, Rubin first used a standard Newtonian approach:

$$\frac{mv^2}{r} = \frac{GmM}{r^2} \tag{1.2}$$

where m is the mass of some particular star in the galaxy, v is linear velocity, r is the distance between the star and the center of mass of the galaxy, M is the mass of the part of the galaxy inside the sphere of a given radius r, and G is the gravitational constant. As simple mechanics predicts, velocity keeps growing within the center of the disk and it falls off in the spiral arms. However, the observed distribution was consistent with flat after eighth kiloparsecs ($\sim$26000 light years).

The flat behaviour could be accounted for by introducing into account a growing dark matter halo within the galaxy. Astronomers were able to reproduce this result with multiple galaxies, such as NGC 6503 and NGC 3196.

1.1.2 Weak-Gravitational Lensing

Weak-gravitational lensing studies provide another strong evidence for the existence of Dark Matter. In general, gravitational lensing occurs when light that travels large distances is distorted by an heavy object placed between the source and the observer.

The deflection angle of the perturbed light is proportional to the mass of the object:

$$\theta = \frac{4GM}{rc^2} \tag{1.3}$$

where theta is the deviation of real angle between the source of light and observer, G is the universal gravitational constant, M is the mass of the object and r is an impact parameter. This approximation for point mass can be applied to galaxies allowing to measure mass-distributions when the position of an emitter is known precisely. In some cases, when an heavy object is located on the same line between source and receiver, radial symmetry allows to observe so-called Einstein rings (Figure 1.2).

However, weak-gravitational lensing can also be used to measured the effects of dark matter halos in far objects like the Bullet cluster. As a result of the merging of two neighbor galaxy clusters, the Bullet cluster was analyzed by scientists using X-ray measurements. The X-ray itself was emitted by hot plasma in the epicenter of clusters' collision [17]. The observation shown in Figure 1.3 revealed that zones of dense baryonic matter are not the same as calculated locations of mass peaks, which can only mean that clusters are dominated with non-lumious matter [29].

1.1.3 Cosmic Microwave Background

A further indirect evidence of dark matter comes from the early ages of our universe and can be found in the Cosmic Microwave background (CMB). First detected in the 20th century by Arno Penzias and Robert Wilkinson, the CMB describes the conditions of the early ages of the Universe. CMB is a remnant electromagnetic radiation from the Big-Bang, which contains crucial information about the composition of our universe. While temperature distribution of the CBM seems to be flat on a large scale, more precise analysis reveals angular fluctuations of temperature in range of 10^{-5}K (Figure 1.4).

Using standard cosmological model, the Plank collaboration [1] studied the energy density distribution as a factor of angular distances (Figure 1.5). Parameter l represents expansion of

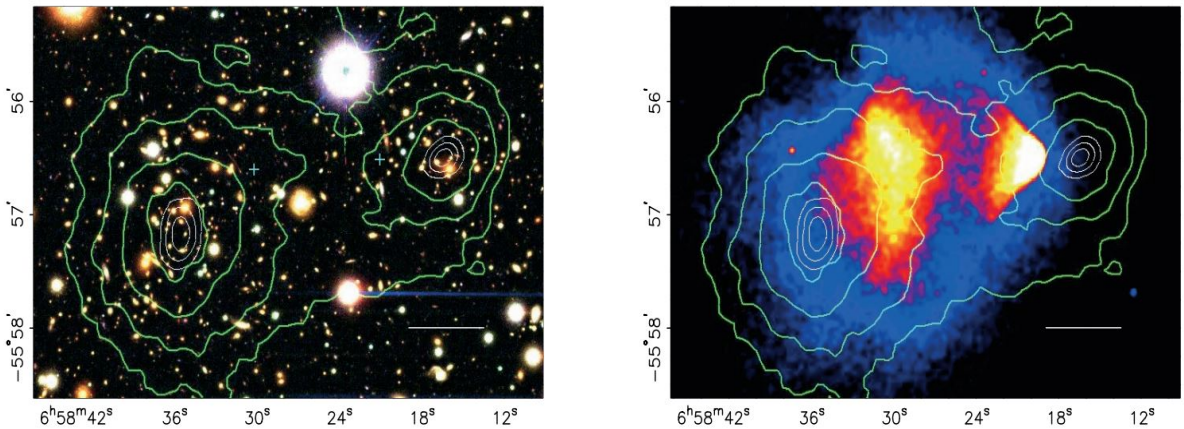

Figure 1.3: Gravitational lensing in the Bullet Cluster [16]. Green lines identify based on gravitational lensing predicted mass distribution, while while X-ray scan (right) predicts concentrated mass locations to be in yellow and red zones

the energy density distribution. The current estimations from the study show that Dark Matter makes up for 25% of the entire universe.

1.2 Dark Matter Candidates

Despite the list of indirect evidences discussed in the previous section, very little is known about Dark Matter. The mainstream theory expands Beyond the Standard Model of particle physics (BSM), with a large number of proposed candidates. However, there are few limits and conditions, which all the dark matter candidates must satisfy:

Non Baryonic, motivated by the lack of interaction with light; Non Relativistic, motivated by large-scale structure of the universe [10]; Long-Lived, the lifetime has to be of the order of the life of the universe for it to be in relic density.

It is impossible to mention every candidate in a huge variety, so the next sections will be focused on the most popular among current theories.

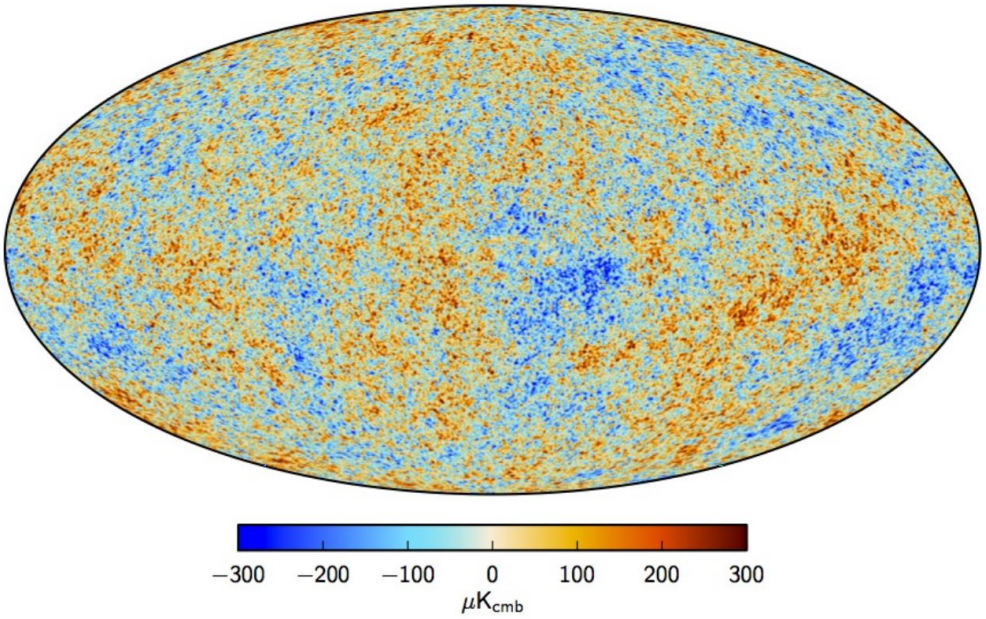

Figure 1.4: Recent results of Planck collaboration on measuring the Cosmic Microwave Background [17]

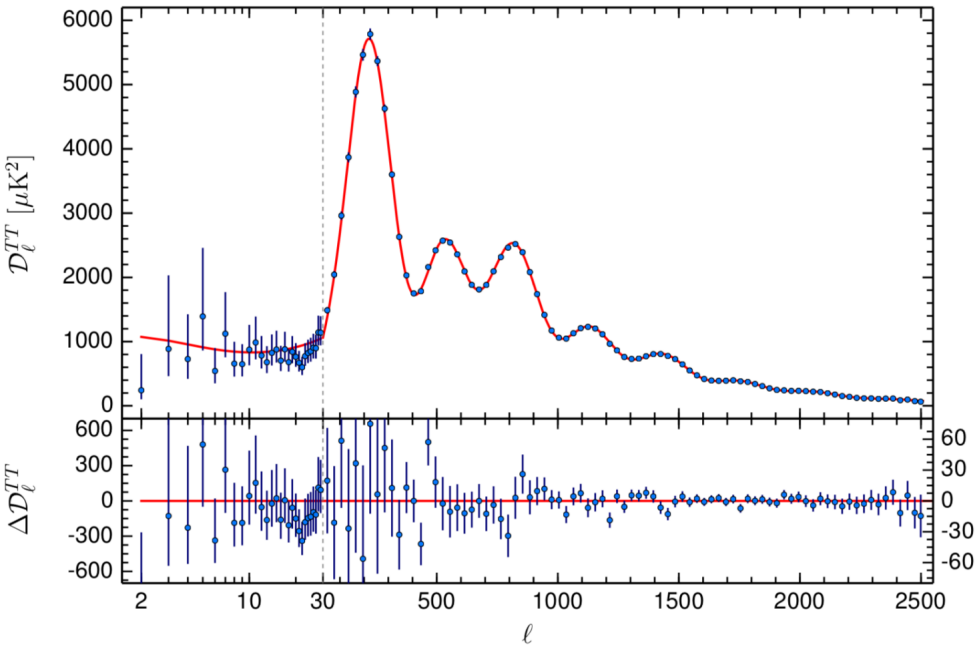

Figure 1.5: Cosmic Microwave Background temperature spectrum measured by Planck collaboration in 2015 [1]. The relative amplitudes at the bottom show the approximate ratio of baryonic matter to dark matter to be 1 to 5.

1.2.1 WIMPs

The current most favourite candidate are Weakly Interacting Massive Particles (WIMPs). From its name, WIMPs interact weakly and have expected masses in the GeV-TeV range [28].

During the early stages of the Universe, WIMPs were in perfect equilibrium between production and annihilation, but as the universe started expanding and therefore cooling, the overall energy would have fallen below the threshold for WIMP production. This effect would have left the relic WIMP abundance that we may observe today [25].

The work put forth in this thesis is focused on directly on WIMPs searches.

1.2.2 Axions

Charge parity (CP) violation remains to be one of the biggest open questions in current Standard Model theory, breaking entire CP-conservation in quantum chromodynamics (QCD). In their attempt of solving one, Peccei and Quinn suggested a new Symmetry (U(1)) [37] for the last term in Lagrangian Eq. 1.4 for QCD, while first two have symmetry (SO(3)):

$$L_{QCD} = -\frac{1}{4}F^{\alpha}_{\mu\nu}F^{\mu\nu}_{\alpha} - \sum_n \bar{\psi}_n \gamma^{\mu}[\partial_{\mu} - igA^{\alpha}_{\mu}t_{\alpha}]\psi_n - \sum_n m_n \bar{\psi}_n \psi_n \tag{1.4}$$

where the first term describes gluon interaction with gluon field tensors, ψ_n is a quark field of Dirac four-spinor, and t_a stays for 8 gluon colour matrices in the second term, describing chromodynamic part of the equation.

This new symmetry requires the existence of a new particle - Axion [42]. Today, the ADMX (Axion Dark Matter eXperiment) is a current leading collaboration searching for this new particle [39]. Using Primakoff effect with a supercondating microwave resonator, they have gradually been narrowing the mass-region of Axions in last several years.

1.3 Detection of Dark Matter

1.3.1 Dark Halo Model

The characteristics of the Dark Matter halo in our galaxy are fundamental to any proposed Dark Matter measurement, as they directly impact the expected rate in our frame. Spherical

dark matter halos are strongly motivated by gravitational lensing and rotational curves measurements. This model predicts the density of the Dark Matter halo ρ_x falls off proportional to r^{-2}, where r is the distance to the galactic center. According to Lewin and Smith, the halo density for Milky Way galaxy varies from 0.2 [GeV/(c^2 cm^3)], to 0.4 [GeV/(c^2 cm^3)], with an average 0.3 [GeV/(c^2 cm^3)] [32]. The simplest physical distribution for this theory would be to assume Maxwellian velocity distribution for the dark matter particles in the halo [32]. Except that, Standard Halo Model (SHM) assumes halo to be isothermal, meaning that its temperature is stable and does not depend on the exact location [31]. Exact parameters of SHM are presented in Table 1.1

Parameter	Standard value
v_0	220 [km/sec]
v_{sun}	232 [km/sec]
v_{esc}	544 [km/sec]
ρ_{halo}	0.3 [GeV/c^3cm^3]

Table 1.1: The main parameters of the Dark Halo Model [21].

1.3.2 Detection Methods

There are many techniques used to probe dark matter. In general these searches can be classified in three groups: direct detection, indirect detection, and production in collisions. Depending on how one reads the Feynman-style process diagram on Fig. 1.6, all three processes can be described qualitatively.

Production in collision is based on generating the same conditions of early stages of the Universe in a laboratory, by colliding particles at high Energies. Accelerated to TeV energies, baryonic particles could create dark matter directly. Traditional collider detectors can measure energies of all the outgoing particles, imbalance of transverse energy after the explosion would mean a loss of energy due to the creation of dark matter, which can not be detected.

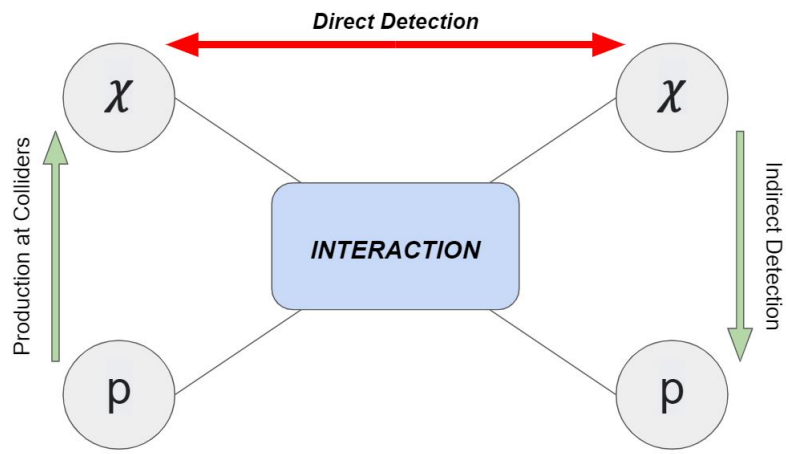

Figure 1.6: Schematic Feynman diagram of three different detection methods based on the initial and final particles, participating in interactions. Dark matter candidates are labeled as χ, and P represents baryonic matter.

Indirect detection is based on annihilation decay of Dark Matter particles that can lead to the production of baryonic matter. Annihilation is proportional to dark matter density squared, and resulting particles can be caught and analyzed with detectors [18].

Direct search of dark matter particles relies on the recoil signal from elastic or quasi-elastic scattering of Dark Matter particles with a target nuclei or electrons [21]. The primary challenge of this method is to separate WIMP-produced recoils from backgrounds in the detector since not only dark matter can produce a detectable signal.

1.3.3 WIMP direct detection

Elastic and quasi-elastic scattering of WIMPs with matter can lead to the production of the following effects in a detector: phonon production, charge production, and photon production.

Since the basic process of direct detection method is recoil kinematics, one can postulate that recoil energy E_r of a target nuclei, scattered elastically with a WIMP particle of mass m_χ and velocity v, can be calculated using Eq. 1.5:

$$E_r = \frac{\mu_r^2 v^2}{m_n}(1 - Cos\theta) \tag{1.5}$$

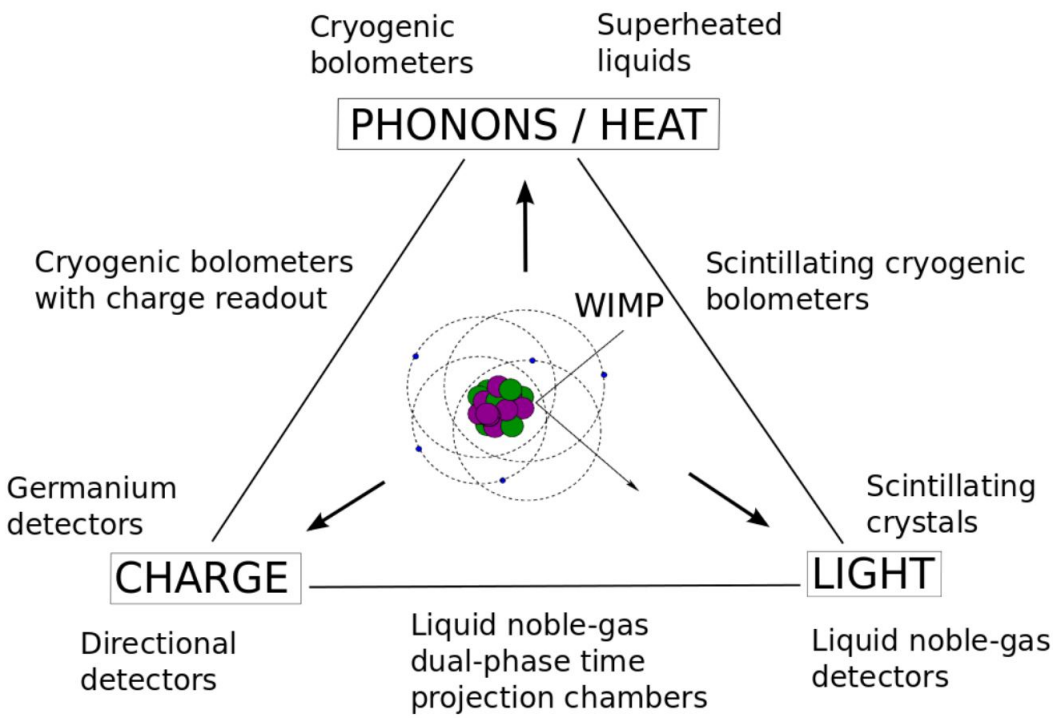

Figure 1.7: Different techniques using for WIMP direct detection [40]

where m_n is target nucleus mass, θ is scattering angle in the WIMP-nucleus centre of mass frame and μ_r is reduced WIMP-nucleus mass:

$$\mu_r = \frac{\mu_\chi m_n}{\mu_\chi + m_n} \tag{1.6}$$

Generally, differential cross-section of the scattering Dark Matter particle can be spin-dependent (SD) or spin-independent (SI), so both terms must be taken into account. In this case, the differential cross-section of WIMP-nucleus can be expressed as

$$\frac{d\sigma_{\chi n}}{dE_r} = \frac{m_n}{2\mu_r^2 v^2}(\sigma_0^{SI} F_{SI}^2 + \sigma_0^{SD} F_{SD}^2) \tag{1.7}$$

where F_{SI} and F_{SD} are form factors for spin-independent and spin-depended term correspondingly, and are functions of the transferred energy. For the SD case the cross-section can be calculated for the total spin of the target nucleus J as following:

$$\sigma_0^{SD} = \left(\frac{32}{\pi}\right) G_F^2 \mu_r^2 \left(\frac{J+1}{J}\right) [\langle S_p \rangle a_p + \langle S_n \rangle a_n]^2 \tag{1.8}$$

with Fermi constant G_F, a_p and a_n to be effective coupling of the WIMP to proton and neutron correspondingly for the SD case, $\langle S_p \rangle$ and $\langle S_n \rangle$ to be the expectation values of spin for

proton and neutron:

$$\langle S_{n,p} \rangle = \langle N | s_{n,p} | N \rangle \tag{1.9}$$

WIMP-proton and WIMP-neutron cross-section limits for SD case can be expressed as following:

$$\sigma_{SD_{n,p}} = \frac{24 G_F^2 \mu_{n,p}^2 a_{n,p}^2}{\pi} \tag{1.10}$$

when only one of two interactions (proton or neutron) is dominated and the second one can be reasonably neglected.

For SI case, WIMP-nucleus cross-section is given by [38]:

$$\sigma_0^{SI} = \frac{4\mu_r^2}{\pi} [Z f_p + (A - Z) f_n]^2 \tag{1.11}$$

where A and Z are atomic mass and atomic number of the target nucleus, f_p and f_n are the effective SI coupling of a WIMP to proton and neutron correspondingly.

1.3.4 Current Status

Currently a large number of experiments cover both the SI and SD WIMP detection channel. No observation has been made in the field. Various experiments have been able to further constrain different combinations of WIMP masses and cross-sections. A list of principle published WIMP exlusion cross-section curves are shown in Figure 1.8. The DEAP-3600 experiment, the focus of this thesis, achieved the best sensitivity among LAr-based experiments.

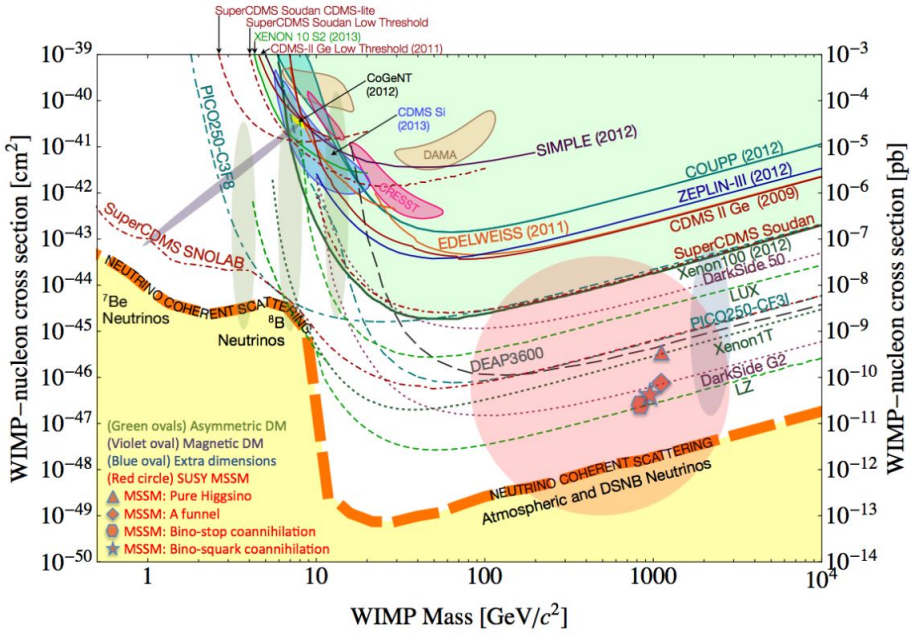

Figure 1.8: Current status of leading WIMP-search experiments. Green section is proved to be forbidden for WIMP parameter space, while current lower limit of the search is set to be a neutrino floor [19].

Chapter 2

DEAP-3600

The Dark matter Experiment using an Argon Pulse-shape discriminator with about 3300 kg of liquid argon (DEAP-3600) is the focus of the work reported in this thesis. The detector is located 2 kilometers underground in an active mine at SNOLAB, in Sudbury ON, Canada [20]. The DEAP-3600 is a single-phase liquid argon (LAr) detector optimized for the detection of spin-independent WIMP-nucleus interactions. The maximum target-medium load of the detector is 3600 kilograms, however, due to post-commissioning hardware issues it currently operates at approximately 3300 kg [12]. The sensitivity of the detector to the WIMP-nucleon cross-section is 10^{-46} cm^2 for a WIMP mass of 100 GeV/c^2 [5]. The main purpose of the experiment is to detect a WIMP directly using scintillation light, which would be produced after a dark matter particle scatters off a target atom in the detector. A further benefit of LAr is the two distinct time-constants of the generated scintillation light: a fast time-constant on the order of a few nanoseconds and a long time-constant on the order of one microsecond, depending on a quantum state of an excited argon dimer. Depending on the nature of the recoil (nuclear or electronic), the population distribution of the quantum states is considerably different, making it easy to distinguish between nuclear recoils and beta/gamma radiation in the experiment.

2.1 Noble Liquids Physics

Although the scintillation method can be applied to other noble liquids, there are still some advantages of using argon specifically. Helium should not be used as a target medium due to its extremely low boiling temperature and comparatively light mass. Other possible candidates are neon, argon, and xenon. The atomic number (Z=18 for argon) plays a significant role in the process of recoils. The higher the density of a medium, the larger the number of target nucleons occupying the same volume, linearly increasing the probability of interaction with traveling particles. Another crucial feature of a noble gas for dark matter searches is a photon yield per deposited energy. Per 1 keV of energy, argon emits 42 photons at zero electric field, which is much higher in comparison to neon's 15 [13] and results in a more efficient detector.

The deciding factor prioritizing argon over xenon is the simplicity of extracting it from the environment. Due to a large portion of argon in the atmosphere, it is relatively easy to get argon from liquid air by distilling. It affects the cost of an experiment drastically. To date, xenon is more than 300 times more expensive than argon, while its scientific benefit is still under discussion.

2.1.1 Liquid Argon Dimers

A dimer is an unstable bound state of two noble liquid atoms in cold temperature. The dimers' decay leads to a photon emission [35], called scintillation light. Emitted light during the dimer decay process has a peak wavelength of roughly 128 nm, being in an ultraviolet (UV) spectrum [27]. Dimers are the resulting products of argon atom excitation, which can be achieved in two ways: recombination and self-trapped excitation [23].

The recombination process is schematically shown in Figure 2.1. First, an argon atom in the ground state interacts with a traveling particle and gets ionized, emitting a free electron. A positively charged argon ion combing with another ground-state argon atom to form an unstable dimer ion. Recombination with a free electron makes the dimer electrically neutral.

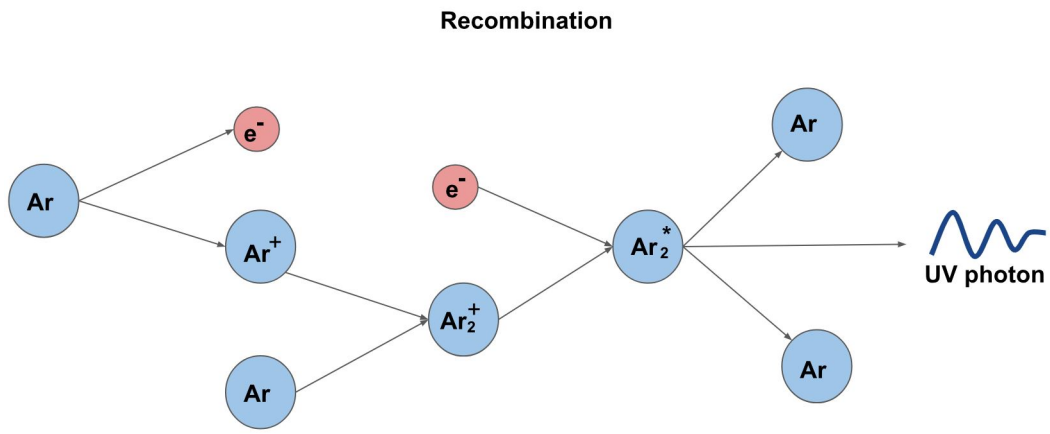

Figure 2.1: Schematic diagram of the scintillation photon emission in the recombination process

The decaying, unstable electrically neutral dimer creates two ground-state argon atoms and a photon in the ultraviolet spectrum to compensate for the difference in energy.

The more direct process of creating a spontaneous dimer is called self-excitation, schematically shown in Figure 2.2. In this process, the interaction of an argon atom with a moving particle and the energy transfer between them causes an excitation of the atom. Two argon atoms in a ground state can not bound together making a dimer, but it can be produced after the interaction between one ground-state atom and one exciton [30]. Again, similar to the recombination process, the unstable dimer decays and emits an ultraviolet photon.

As described before, dimers can be produced by excitation but also by the recombination of electrons and ions especially when the density of ionization is high, which is the case for nuclei energy deposition. Therefore the recombination process will boost the scintillation yield of nuclei compared to electrons. On the other hand, dimers can decay non-radiatively due to dimer-dimer interaction or interactions with excited atoms. This process suppresses scintillation when the density of dimers is high, which again is much higher for nuclei than electrons. This process suppresses scintillation light production by nuclei. Furthermore, the time scale of non-radiative de-excitation are comparable to the scintillation time scale and they suppress the

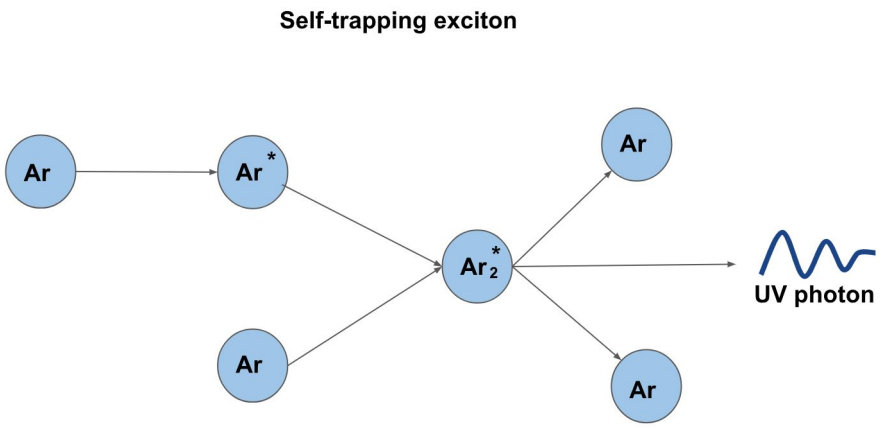

Figure 2.2: Schematic diagram of the scintillation photon emission in the excitation process

long lived triplet dimer much more than the short lived singlet dimer. Overall the results is that electrons traveling in LAr will yield a lot more late photons due to triplet dimer decays than nuclei.

2.1.2 Pulse Shape Discrimination

A liquid argon dimer produced using any of the methods described above can only be in one of three states: one triplet and two singlets. The parity conservation principle does not allow one of the singlet states to emit scintillation light in the process of a dimer decaying down to two ground-state argon atoms [6]. The lifetimes of the other two decay states are very distinct, and this is the main principle of the Pulse-Shape Discrimination (PSD) method. The triplet state decay is carried out over 1.6 μs while the splitting of a singlet exciton into two atoms happens during a much shorter time of 7 ns [27]. Fortunately for the WIMP detection analysis, there is a direct correlation between the probability of creating a singlet or a triplet dimer state and the characteristics of traveling particles, whose energy transfer leads to an excitation [5].

For this reason, one of the main parameters in the DEAP-3600 light detection process is F_{prompt}, which identifies the ratio of the amount of a prompt light to the total amount of detected

light during one event, i.e., the interaction of LAr with one traveling particle:

$$F_{prompt} = \frac{\gamma_{prompt[150ns]}}{\gamma_{total}} \tag{2.1}$$

where $\gamma_{prompt[150ns]}$ represents the amount of light recorded in the first 150 ns of a particular event and γ_{total} is the total amount of detected light. This crucial feature for a new particle detection method was proven to be extremely efficient in a previously conducted DEAP-1 experiment [22].

2.2 Detector Design

There are a few basic principles and challenges of building such a large detector. First of all, since the expected WIMP interaction rate is tiny, a proper calibration system must be designed, implemented and tested, in order to be able to reconstruct each event independently using reconstruction methods and probability algorithms. When reducing the dominant background sources of both the NR and ER events, radioactive shielding construction is used to isolate the fiducial argon from external background sources, while careful material selection mitigates internal radiation from each detector part. It is also necessary to collect as many photons as possible using high efficiency sensors and reflecting materials. This section briefly describes the motivations behind and realization of the essential hardware parts in the DEAP-3600.

2.2.1 Inner Detector

A schematic cross-section of the detector is shown in Figure 2.3 and a list of key parameters is shown in table 2.1. The inner detector consists of a spherical acrylic vessel (AV) with an 85 cm inner radius and 5 cm thickness. Acrylic material is well suited for this purpose not only because it is clean, both optically and radioactively, but also because it can shield the medium from external neutron background [3]. Besides AV, acrylic cryostat includes 255 acrylic light guides, extending 45 cm in length and 19 mm in thickness, connecting the AV

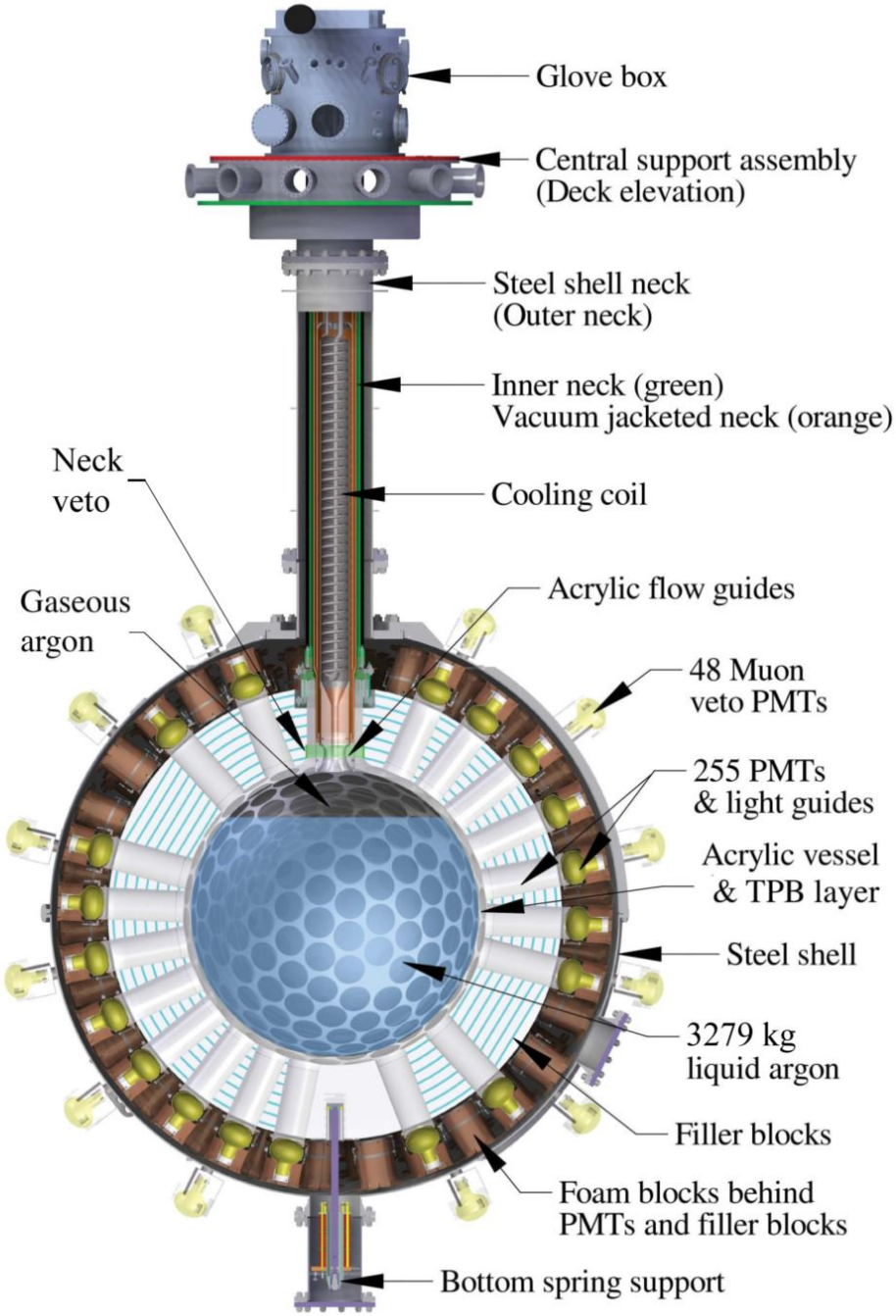

Figure 2.3: Cross-sectional diagram of the DEAP-3600 detector [3]. The lower sphere is filed with approximately 3300 kg of liquid argon. Cooling and filling systems are realized using a vertical neck cylindrical part.

with 255 Hamamatsu R5912-HQE photomultiplier tubes (PMTs) for complete light detection. The light guides shield the inner detector from PMT glass radioactivity and allow operating the

Figure 2.4: Acrylic vessel (left) and copper shielding (right) in the process of installation

PMT close to room temperature. The light guides cover approximately 75% of the total AV surface area.

Having light reflectors around the AV is important for the DEAP-3600 detector. Reflectors prevent photon leakage in between light guide, hence maximizing light collection.Diffusive reflectors cover the outer surface of the AV to bounce photons back into the LAr until they get trapped into one of LGs [3]. Specular reflectors surround the LG surface salvaging a fraction of the photons escaping from the light guides. A 150 μm aluminized mylar foil was chosen as a reflector material. Thin copper shields surround the LGs, and the space between them is filled with polyethylene and Styrofoam materials [3] providing both neutron shielding and temperature isolation.

Inside a thin spherical stainless steel vessel is where the inner detector is placed. The vessel provides a connection to the inner detector from the outside through a vertical cylindrical neck. A cooling coil inside the neck uses liquid nitrogen for keeping the argon in a liquid state. On its top, the neck part has a glove box construction. The whole stainless steel installation is submerged into a 7.8-meter diameter tank. The tank is filled with ultra-pure water, shielding the inner detector from external gamma ray radiation and enabling the detection of cosmic muons. For precise muon detection, 48 outside-looking Hamamatsu R1408 muon veto (MV)

Parameter	Specification
Radius	85 [cm]
Total argon mass	3300 [kg]
Water shielding tank volume	375 [m^3]
Number of inner detector PMTs	255
Number of Cherenkov veto PMTs	48
Light yield	About 8 [N_{pe}/keV]
Sensitivity around 100 GeV/c^2	10^{-46} [cm^2]

Table 2.1: The main parameters of the DEAP-3600 detector [3].

PMTs are located on the outer surface of the stainless steel frame, scanning the light inside the water shield [3].

The wavelength of scintillation light in liquid argon is in a vacuum ultraviolet spectrum (VUV) with a 128 nm peak [15]. This wavelength corresponds to lower photon energy than the energy of the argon's first excited atomic state. It prevents photons from being absorbed by LAr in AV. Thus, every interaction which happened in the inner detector leading to the creation of a dimer can be detected and reconstructed.

For converting VUV photons into visible light and further detection by PMTs, a thin-film wavelength shifter was deposited onto the inner surface of the AV. Organic 1,1,4,4-tetraphenyl-1,3-butadiene (TPB, $C^{28}H^{22}$) covers the total internal area of the AV with a layer thickness of nearly 3 μm [14]. After interacting with TPB, 420 nm photons travel in the AV and then get detected by PMTs.

Since the PMT's efficiency is dependent on its temperature, sixteen PMTs have a temperature sensor installed on the copper parts of the light guides. Copper shields surround every PMT to equalize the temperature along the photodetectors. Sensors are distributed evenly among LGs so that the approximate temperature for each specific PMT can be accurately estimated based on the readings of surrounding sensors.

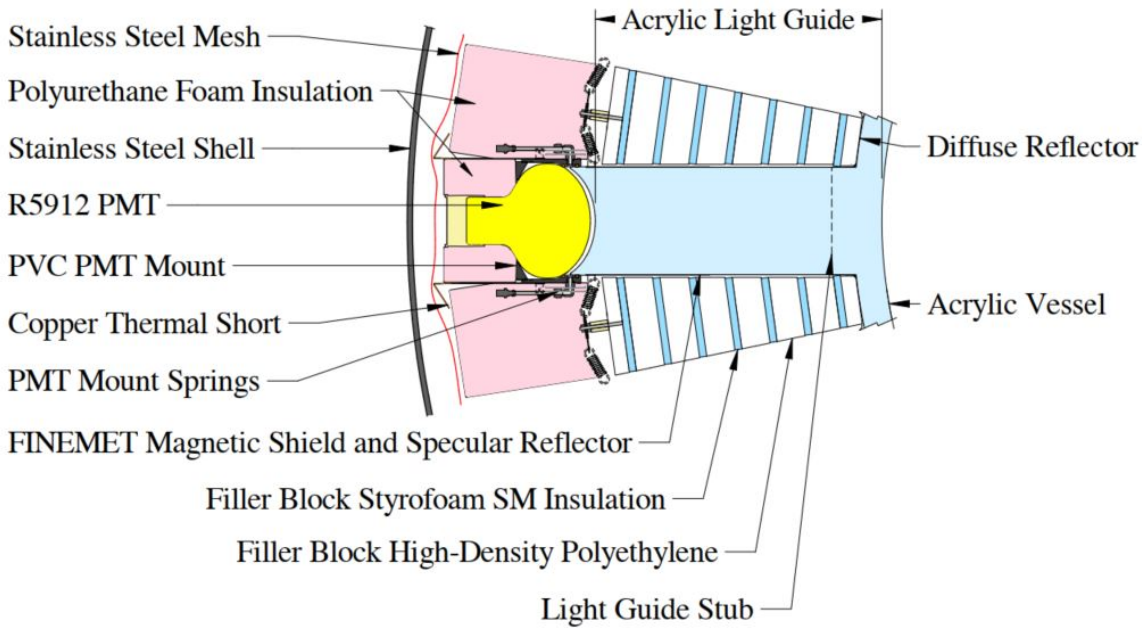

Figure 2.5: Schematic cross section of the inner Hamamatsu PMT coupled to the acrylic vessel [3]

The way a PMT is connected to a light guide is shown in detail in Figure 2.6. Optical coupling is achieved between the PMT and LG by using Sigma Aldrich material (378399) to fill the entire intermediate space of the PMT-LG system [3] inside a cylindrical barrel. The material was chosen because of its glass-imitating optical parameters and because it satisfied thermal conduction parameters. A copper sleeve with a high index of thermal conductivity eliminates thermal fluctuations along the assembly and prevents possible temperature instabilities. A FINMET [8] shield around each PMT lessens the effect of background magnetic fields.

2.3 Radioactive Backgrounds

Various background source may mimic wIMP interactions. Background signals from all the surrounding radioactive sources must be estimated, identified and removed. Therefore, reducing radioactivity is vital for the experiment. Corresponding parameters must be taking into account in the design, which requires a proper material selection. In this way, sensitivity to

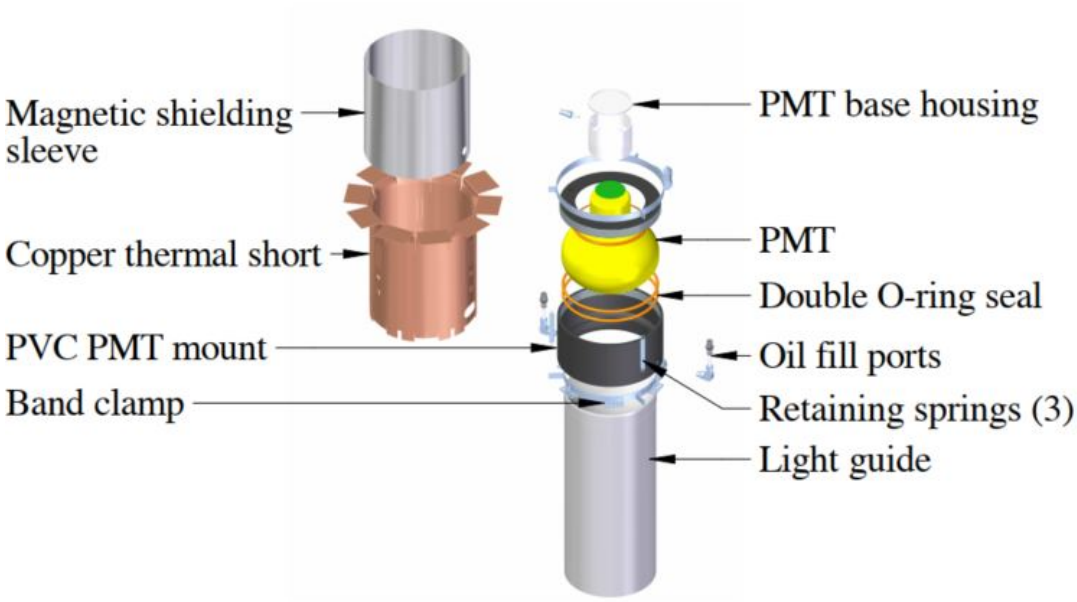

Figure 2.6: Detailed design of PMT and light guide connection [3]

WIMP cross-section can be maximized.

There are some sources of background signals which might look like predicted WIMP events. Among them are radon decays within an argon medium, material radioactivity of the acrylic in the inner detector, ^{39}Ar beta decay, neutron background, and cosmic background.

2.3.1 ^{39}Ar Beta Decay

As mentioned before, one of the reasons for using argon for the dark matter search is the simplicity of its extraction from the atmosphere. However, it also means that stable ^{40}Ar carries unstable ^{39}Ar isotopes (with a 269 year lifetime) as a result of interaction with cosmic rays [33]. Stable potassium ^{39}K is a final product of ^{39}Ar β-decay, which also produces a free electron and electron anti-neutrino particle:

$$^{39}Ar \rightarrow {}^{39}K + e^{-} + \bar{\nu}_e \tag{2.2}$$

In natural argon, the frequency of isotope decay is estimated to be roughly 1 Bq/kg [9]. Assuming this number to be constant due to its long lifetime, the DEAP-3600 experiences around

3300 ^{39}Ar β-decay events per second, or 285 million events per day. This rate can be diminished by extracting argon from underground deposits or using various distillation techniques. Nevertheless, this dominant background can be reduced entirely using a PSD method described in section 2.1.2, based on previous studies of a previously completed DEAP-1 experiment [5].

2.3.2 ^{238}U and ^{232}Th Alpha Decay Chains

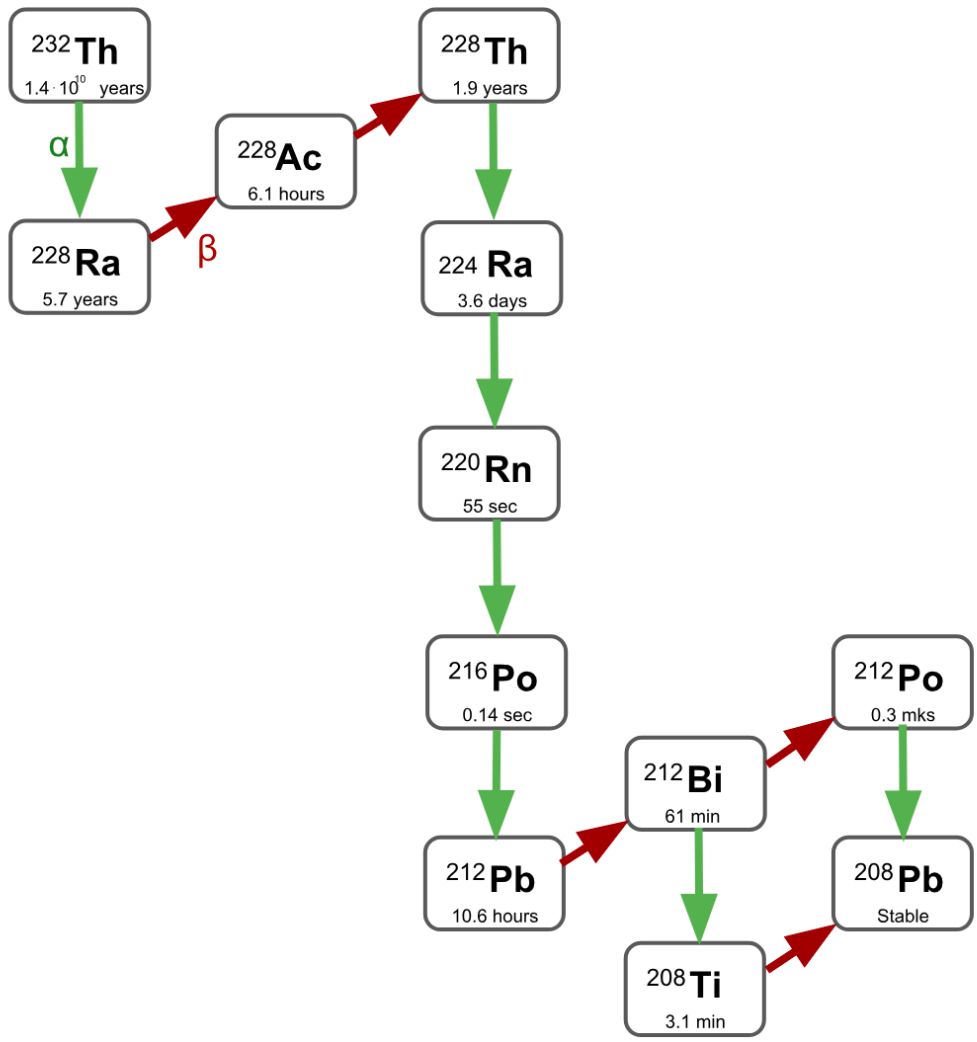

Figure 2.7: Thorium decay chain, including lifetimes of all the intermediate particles. Alpha decays are labeled in green, beta decays are labeled in red

The main sources of unstable particles with lifetimes comparable to the age of the earth ($\sim$10 billion years) for the DEAP-3600 are ^{238}U and ^{232}Th decay chains. These chains mix

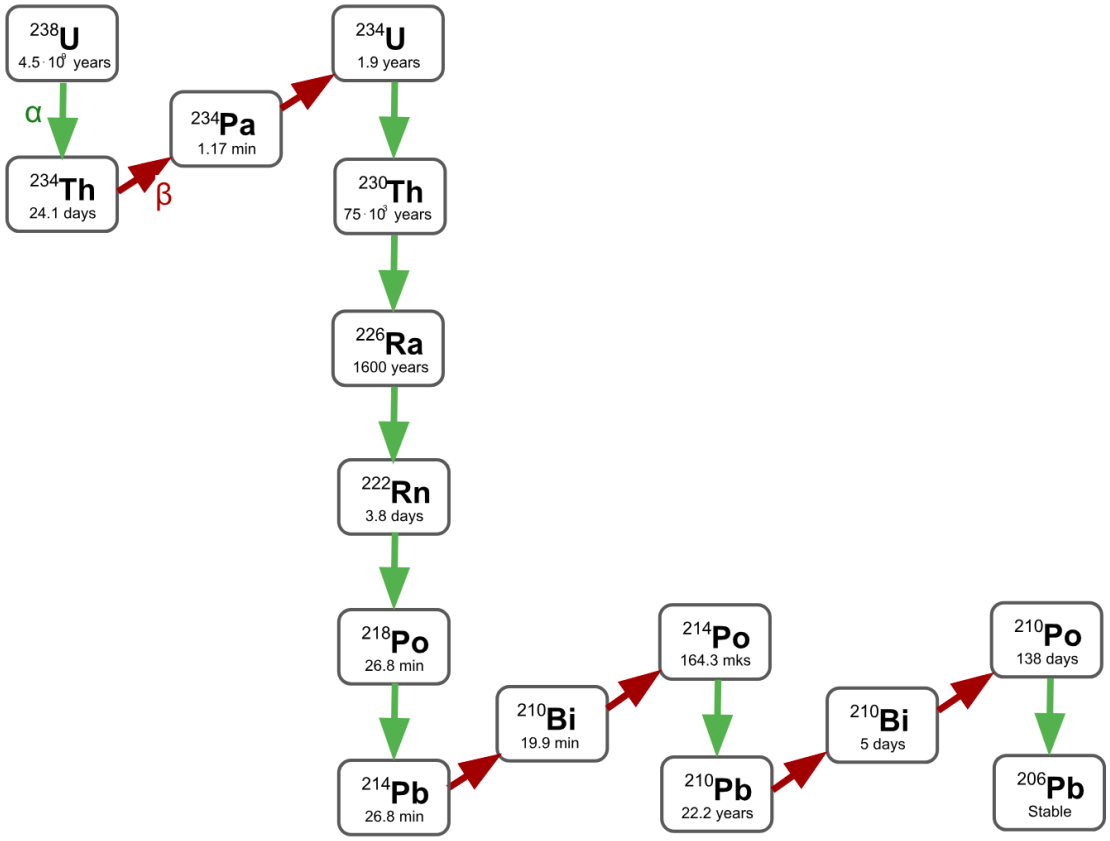

Figure 2.8: Uranium decay chain, including lifetimes of all the intermediate particles. Alpha decays are labeled in green, beta decays are labeled in red

both α- and β-decay processes, emitting a significant number of electrons and alpha particles. Helium nucleus similarly interact with LAr as argon nuclei do, mimicking scintillation events. In both ^{238}U and ^{232}Th decay chains, starting with ^{220}Rn and ^{222}Rn correspondingly, daughter isotopes have a short lifetime and high energies (approximately a few MeV) of emitted particles [36]. Despite the similarity of F_{prompt} parameters of the events with predicted WIMP interactions, these events can still be separated because their energy deposited is much higher than WIMP interactions. However, in the case that a radioactively emitted ^{4}He nuclei loses a significant part of its energy before entering the LAr volume, it can be classified as a WIMP ROI event. Those events are called surface alpha events.

Surface alpha events might occur in three regions: the acrylic vessel, the TPB and the LAr detector. All possible ways of losing energy by alpha-particles before interacting with

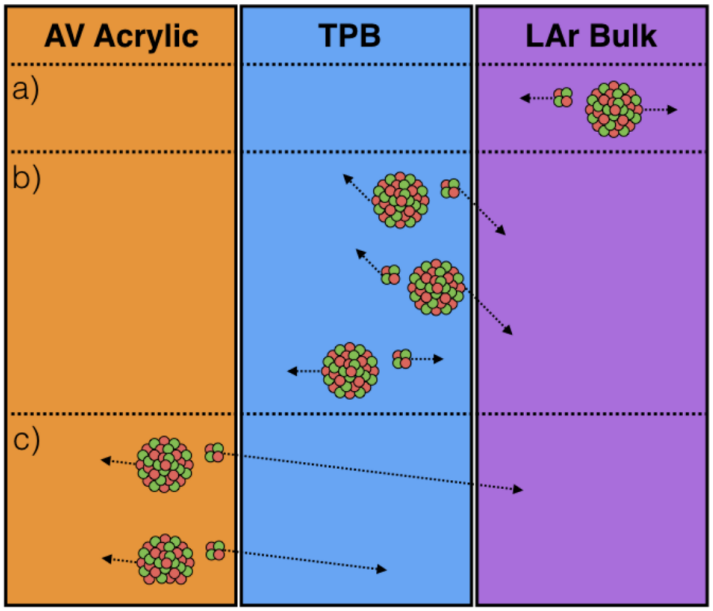

Figure 2.9: Schematic diagram of possible surface alpha radioactivity events [3]

the LAr are shown in Figure 2.9. In the LAr volume, both daughter and alpha particles will generate too many scintillation photons be classified in the WIMP ROI. In the case of alpha decay happening inside the TPB layer, fewer photons are produced though the TPB itself may produce scintillation photons. Finally, decay within the acrylic radiation may generate just enough energy to enter the ROI and be classified as WIMP. Position reconstruction is the only way to identify and reject radon decay daughters on the surface of the AV or within the TPB.

2.3.3 Neutron Backgrounds

Another type of background which might produce the same signal parameters as a WIMP is neutron radiation. It is especially important for this type of experiment to lessen the effect of interacting neutrons. The main sources of this flux are natural reactions in surrounding rocks, cosmic muons, and the PMT glass material. Light guides and filler blocks, implemented around PMT tubes and described in section 2.2.1, drastically suppress neutron background. Spallation neutrons produced by cosmic muons can be rejected by detecting the muon induced Cherenkov photons in the water tank system. Since the DEAP-3600 setup is fully submerged into 500 tons

of ultra-pure water, incoming muons emit Cherenkov light [34], which is observed by 48 muon veto PMTs. Engineering solutions allow keeping a stable temperature and fast water flow in the tank for more accurate light detection.

2.4 Data Collection

Due to having hundreds of sensors recording the data continuously, data analysis is another important part of the project. The motivation of the whole project is to gather statistics of interactions in the region where WIMP scattering can occur. Thus, it is crucial to select physical data properly, applying low-level data cleaning cuts, automatically rejecting all the possible hardware issues and irrelevant signals.

2.4.1 Region of Interest

There are two physical parameters, defining the small window of the region of interest (ROI) for the DEAP-3600: F_{prompt} and the recoil energy of a candidate WIMP-event. Setting the criteria of these values yields a selection of potential WIMP interactions among a variety of detected signals. Since interactions between dark matter and LAr yield nuclear recoil events, electron recoil event can be suppressed. The study of the DEAP-1 experiment was based on the AmBe radiation source. Radioactive ^{241}Am emits alpha-particle, which can be captured by ^{9}Be nucleus. As a result of this interaction, the AmBe source emits photon and neutron. The study showed the variation of F_{prompt} for NR events between 0.7 and 0.9, proving that NR events have much higher F_{prompt} in comparison with ER's $\sim$0.3 [5].

The region of interest is shown in Figure 2.10, having low recoil energy and high F_{prompt}. It allows to diminish the expected rate of argon background events to be 0.2. The lower PE parameter is set as 80 PE (10 keV) to reject argon beta-decay events to a fraction of 0.5, while the higher bound of 240 PE separates the ROI from surface alpha-decay events. Less then 10% of NR events are outside the ROI after applying the framework which is a reasonable

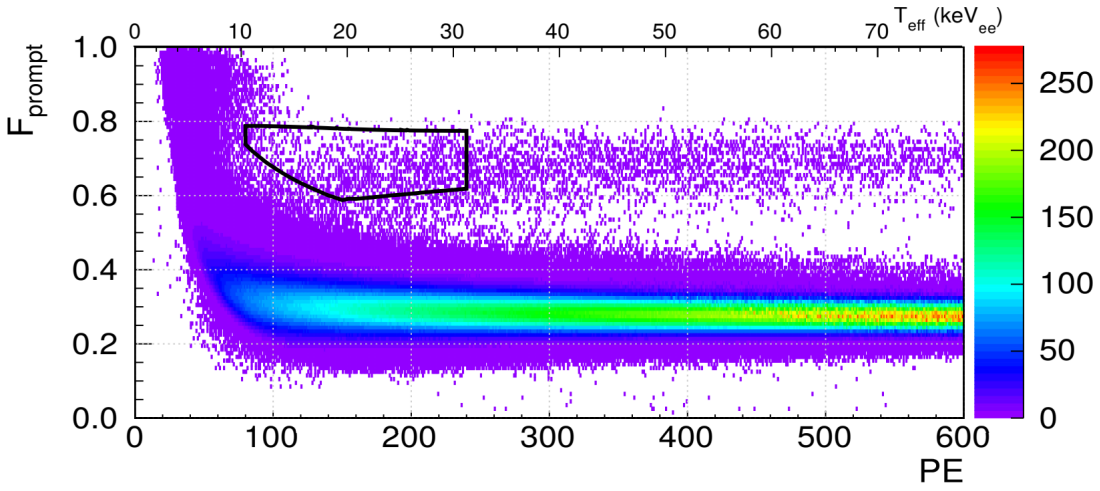

Figure 2.10: Fprompt versus recoil energy parameter space for the DEAP-3600 [2]. Data for 64 h AmBe NR events. The boundaries of the ROI are shown in black. All data-quality cuts are applied.

compromise.

Targeted number of a 3-tonne-year fiducial exposure is 30 neutron events in the ROI, together with 150 surface alpha events and 1.6 billion events of gamma or beta ^{39}Ar decay [3].

2.4.2 Data Acquisition System

All signals from the PMT detectors are digitized in order to enable identifying individual PMT pulses with a timing resolution limited by the PMT transit time spread of about 1ns (σ). The main criteria for the DEAP-3600 Data Acquisition System (DAQ) is to detect all possible very rare WIMP signals without being swamped with the dominant ^{39}Ar background events. The data flow architecture for the DEAP-3600 is shown schematically in Figure 2.11. A WIENER MPOD crate powers the PMTs with a high voltage module. The PMTs convert a signal from photons into an analog pulse. The PMT response is described with more details in Section 3.1. All PMTs are connected to signal conditioning boards (SCB). There are 27 SCBs with 12 channels each, supporting LAr, muon veto and veto neck PMTs. A Digitizer and Trigger Module (DTM) analyzes the analog signals produced by summing the 12 PMT signals within

the SCBs connected to the LAr PMTs. The DTM produces trigger signals that are used to select when to acquire data with the digitizers CAEN V1720s and V1740s. 250 Mega sample per second (MS/s) V1720 boards are used for most data providing dynamic range between 1 and about 60 photo-electrons. 62.5MS/s V1740 digitizers are used when the V1720s saturate mostly for alpha-decays of radon[3]. Test pulses fed into each SCBs are used to measure the timing offsets between digitizers. The DTM generate both clock and a trigger signals ensuring synchronization of the digitizers and calibration systems.

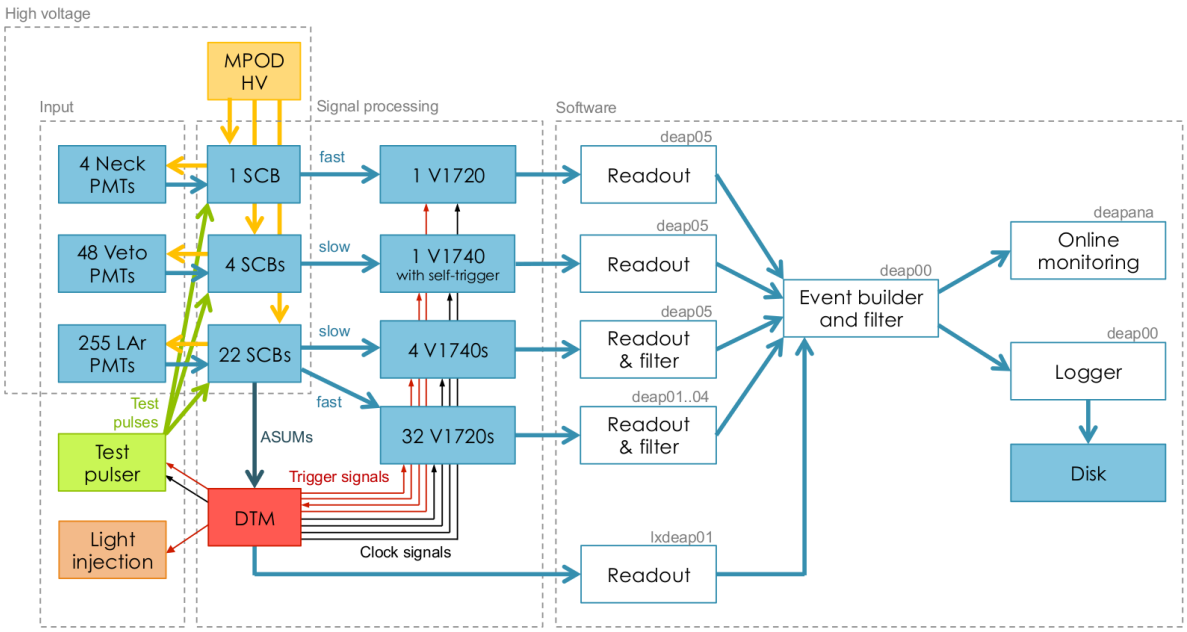

Figure 2.11: Data flow architecture for DEAP-3600 [3]

Chapter 3

Optical model

3.1 Hamamatsu R5912 Photo-Multipliers

The Hamamatsu R5912 8 inch diameter, High-Quantum-Efficiency (HQE) Photo-Multiplier Tubes (PMTs) are devices capable of measuring individual photons. These 255 devices are the core of the DEAP-3600 experiment, as they measure the LAr scintillation light (converted into visible by the wavelength shifter) from interactions that occur inside the detector. The design of these PMTs is shown in Figure 3.1. An 8-inch 700-gram bulb consists of a borosilicate glass window, bialkali photocathode, eleven dynodes and an anode. When an incoming photon is absorbed within the photocathode material on the inner part of the PMT glass, a photo-electron may be liberated. The electric field set between the photocathode and first dynode extracts the photo-electron into the vacuum space where it is subsequently accelerated towards the first dynode. For DEAP-3600, a series of eleven dynodes amplify the signal by increasing the number of electrons after each dynode stage. Each dynode is a metal plate under high voltage covered with a material with a high electron emission coefficient, which is critical for creating avalanches. The total charge is collected at the anode. The avalanche process enables the detection of single electrons by converting single photo-electron into a million of electrons.

The PMT quantum efficiency is the probability that an impinging photon generates a photo-electron and consequently a readable signal. This process depends on the photon wavelength.

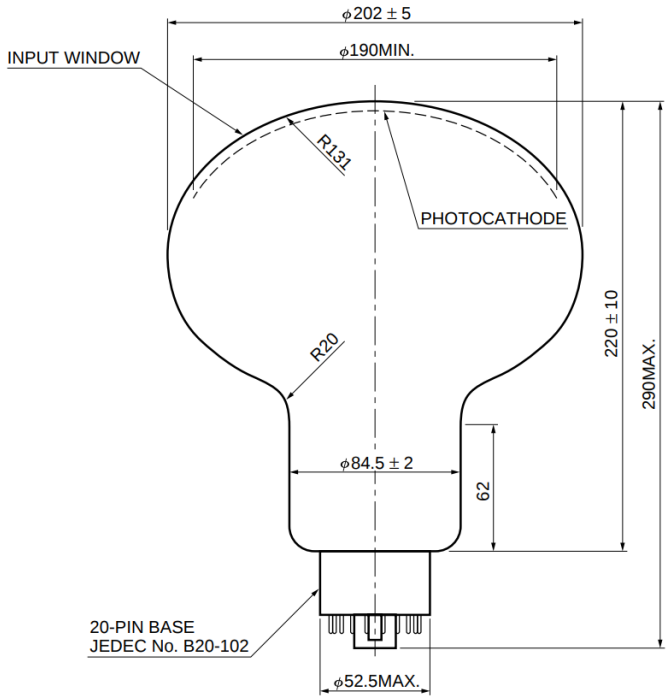

Figure 3.1: Crossectional drawing of the R5912 Hamamatsu HQE photomultiplier tube. The active photocathode area is approximately 530 cm^2 [26]

The peak of the quantum efficiency for the Hamamatsu R5912 is approximately 420 nm. It is much higher than the VUV argon scintillation spectrum that is peaked at 128nm. At that wavelength photons are not detected by any optical device used in the experiment. Therefore using a wavelength shifter is essential for detecting the liquid argon scintillation light. Furthermore the VUV light does not go through acrylic and the wavelength shifting must be deposited on the inside of the acrylic vessel. Figure 3.2 shows the PMT's quantum efficiency as a function of an incoming light's wavelength.

The Hamamatsu R5912 was chosen for DEAP-3600 due to its size, relatively low intrinsic radioactivity, and high quantum efficiency.

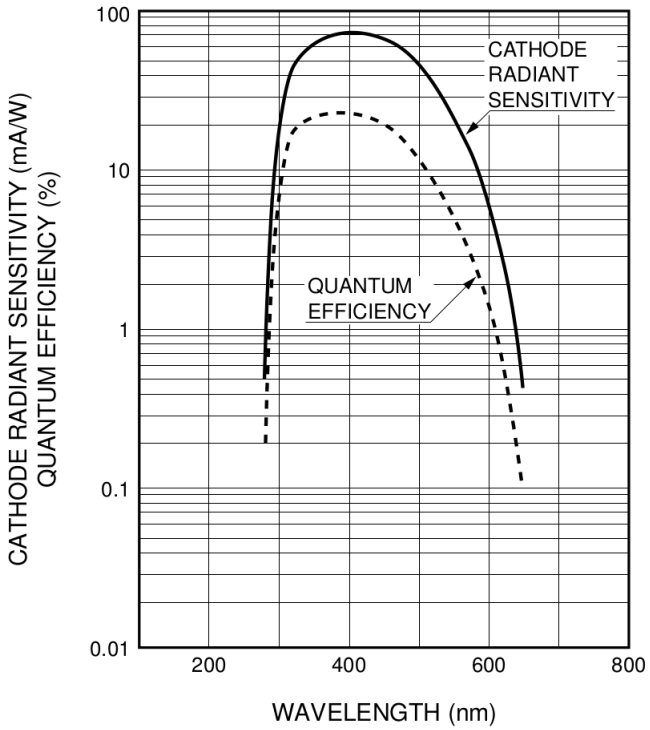

Figure 3.2: Quantum efficiency of the R5912 Hamamatsu HQE photomultiplier as a function of the incoming photon's wavelength

3.2 AARF Calibration System

There are twenty-two light injection sources based on light emitting diodes (LED) implemented in DEAP-3600 for PMT and optical calibration, twenty of which are distributed equally and symmetrically around the detector. The other two are located in the neck part. The aim of this system is in part the calibration of optical parameters of AV, TPB and LAr including their variations over the detector. The Acrylic and Aluminum Reflectors and Fibre-Optics system (AARF) is the combination of a 445 nm LEDs, LED driver system and optical fibers transporting photons to the edge of the light guides with minimum losses. The light from each AARF fiber is reflected onto a PMT using an aluminum mirror as shown in detail in Figure 3.3. A small fraction of the photons, which is approximately 20% of the incoming light, is reflected on the PMT window and redirected towards the acrylic vessel. The so-called AARF's PMT detects the rest of the light. Some of the reflected light gets trapped inside the acrylic, bouncing in the material between the reflector system on one side and the TPB layer on the other

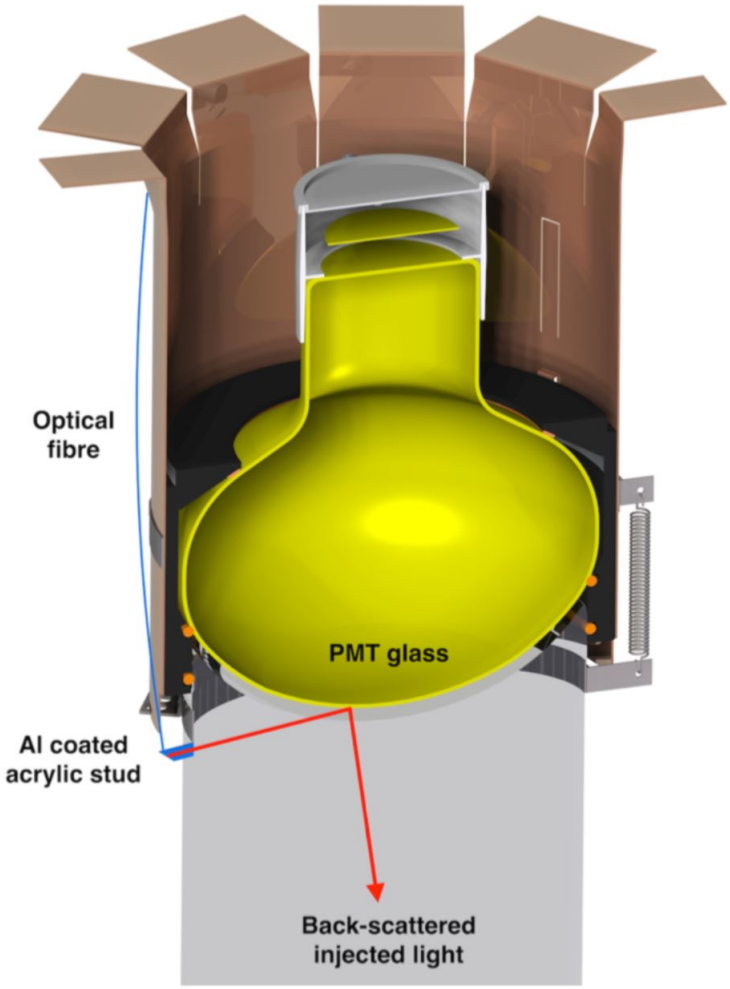

Figure 3.3: AARF method of light injection into an acrylic vessel [4]

side. Bouncing photons are also detected by the AARF's PMT if they bounce back into LG after reflecting from the AV surface, or possibly with one of the neighboring PMTs. A typical distribution of the detected amount of light over the PMTs are shown in Figures 3.6 and 3.7.

The main advantage of using optical calibration with AARFs is the ability to run the calibration process at any time during the detector construction. It makes it possible to compare optical parameters of the inner detector with different settings and properties, such as the presence or absence of a TPB layer. Also, it makes it possible to measure the relative quantum efficiency of each PMT over time, which is essential for data analysis.

While working in the calibration mode, AARFs inject the light into the system in short pulses. The DAQ system creates a trigger for the PMT's data collection, which copy provokes LED light emission. Each light flash counts as one event, during which a signal from every PMT is recorded and collected with the DAQ. The intensity of each AARF light source can be tuned from zero to a few hundred photons per event.

When working with PMT data, one crucial parameter of each PMT is occupancy. It is defined as the ratio of a number of LED flashes during which a PMT detects at least one photon over the total number of events during the calibration data run:

$$Occ[PMT_i] = \frac{N^{ev}_{detected}}{N^{ev}_{total}} \tag{3.1}$$

This number identifies the percentage of the events during which PMT[i] detected at least one photon. Usually, the AARF's intensity is tuned in such a way that most of the PMTs have around 5% occupancy. However, even though 95% of the events do not have photons getting to a PMT[i], there is still a small probability that two or more photons will get the PMT[i] during some event. This probability can be estimated with Poisson statistics:

$$P(N,\lambda) = \frac{\lambda^N e^{-\lambda}}{N!} \tag{3.2}$$

where P(N,λ) is the probability of detecting N photo-electrons by some PMT and λ is the mean number of photo-electrons observed by the same PMT for a certain AARF intensity:

$$\lambda = -ln(1 - Occ[PMT_i]) \tag{3.3}$$

Equation 3.3 represents the relationship between the mean PE number detected by a PMT and its occupancy. A standard occupancy distribution over 255 PMTs is shown in Figure 3.4, together with its distribution over rearranged PMTs based on the distance from the light source. Thus, for 5% PMT occupancy only 2.5% of detected events record correspond to multiple PE events. After three circles of neighbor PMTs, corresponding to a 60 degree opening angle from the AARF, all PMTs record approximately the same occupancy. Photons detected by the PMTs around the AARF source have most likely been reflected at the acrylic vessel (or wavelength

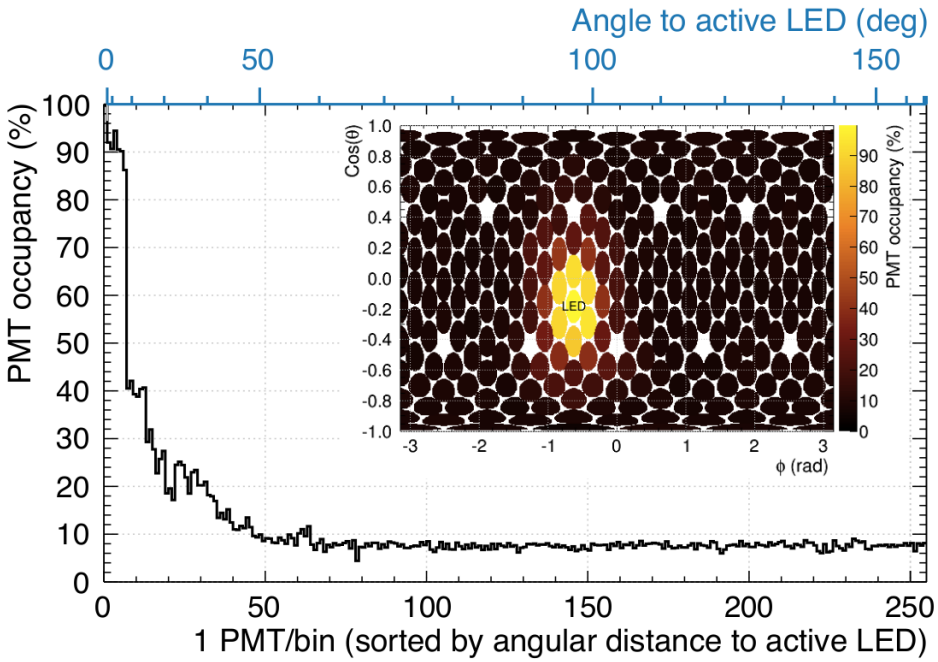

Figure 3.4: Occupancy distribution among PMTs when one of the AARFs is fired [4]. Data for approximately 2 million events.

shifter) interface. Photons detected by the PMT further away from AARF are maximally scattered, as all information about the source location has been erased. Such photons may have travelled along the acrylic vessel or traversed the inner volume of the detector.

3.3 Argon Boundary

Optical properties of a liquid/gas argon boundary have not been described in detail yet. Some attempts of characterization are described in this chapter together with a comparison of the data with simulations.

In the perfect case, the best way to study exactly how the surface between liquid and gaseous argon changes along the Z-direction would be to examine an AARF light source located horizontally at the equator of the acrylic vessel. Then, comparing the optical parameters of the half-filled vessel at slightly different levels and subtracting the signal difference in pulse

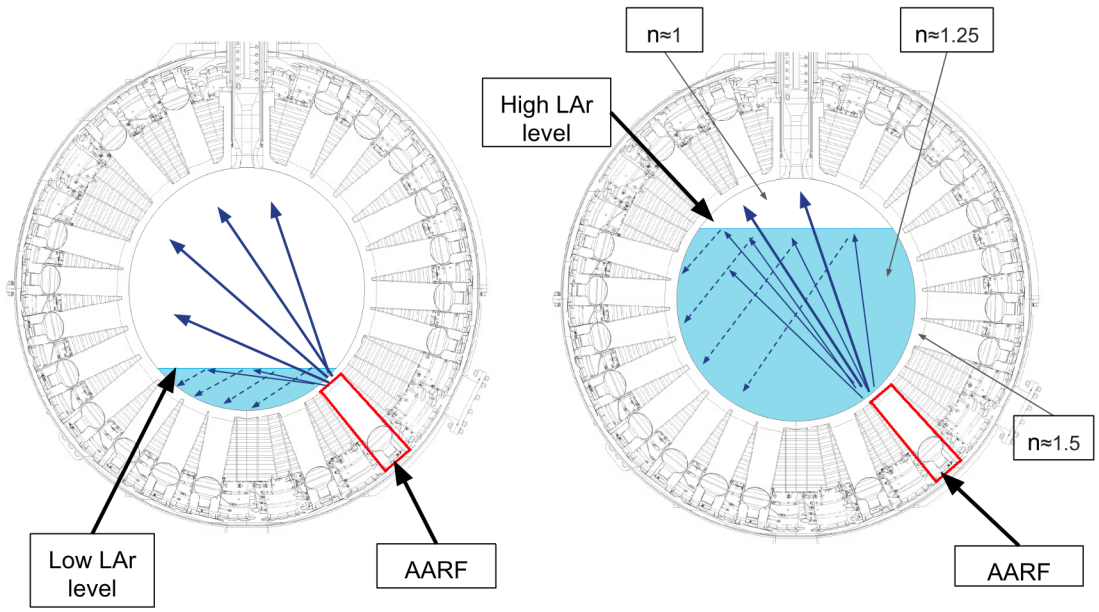

Figure 3.5: Schematic diagram of light injection inside the AV and argon reflection processes with low and high LAr levels

distributions, a detailed analysis could be done. Since such an AARF light injector does not exist in the DEAP-3600, alternative solutions must be found. One of them is using bottom AARF and studying the interaction of an almost vertical photon beam with the surface.

Since a significant number of PMTs are located above the LAr level in the acrylic vessel, the liquid/gaseous boundary has a significant impact on recorded signals and photon distributions in the upper part of the detector. The purpose of this investigation is to analyze different levels of LAr when one of the bottom AARFs is fired. The index of refraction of liquid Argon is significantly higher than gaseous argon and Fresnel equations are expected to apply though the liquid-gas interface may not be flat. A schematic representation of the effect of the liquid-gas interface is shown in Figure 3.5.

For each of the 255 PMTs, the value of the mean charge per event was processed independently for a 40 nanosecond time window at the trigger time.

On every charge distribution plot, no matter what the LAr level is, a significant amount of the light never gets inside the liquid. It is caught inside the acrylic and TPB layers, reflecting internally on the walls back and forth until it is detected by one of the nearby PMTs (the green

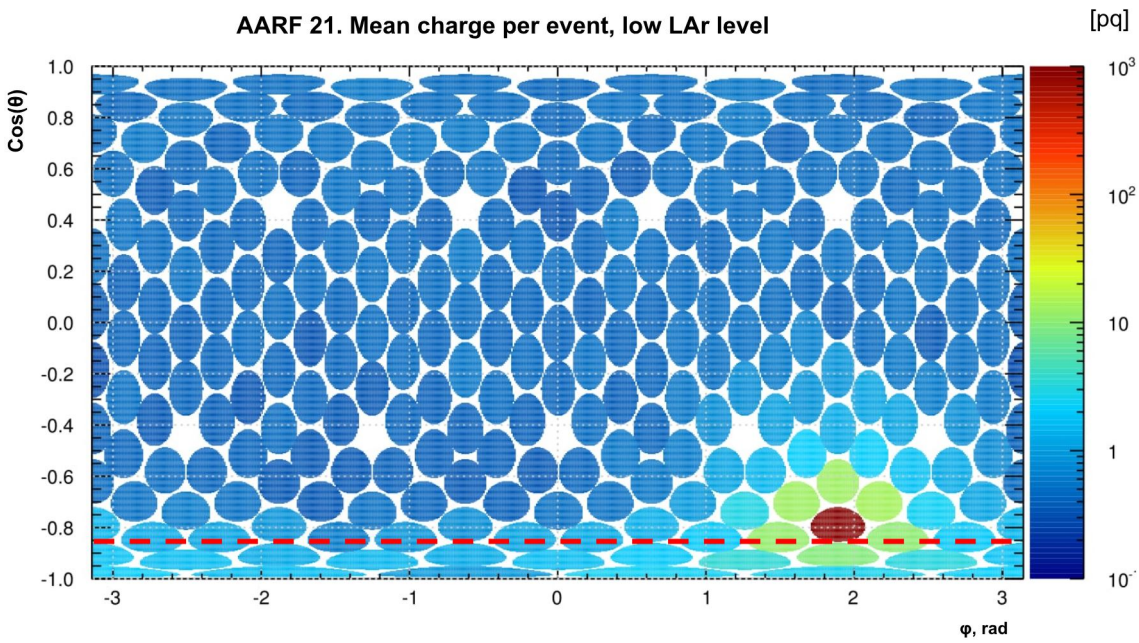

Figure 3.6: Light distribution for low LAr levels (indicated with red line)) with a light source at the bottom of the vessel. Statistics for 500K events

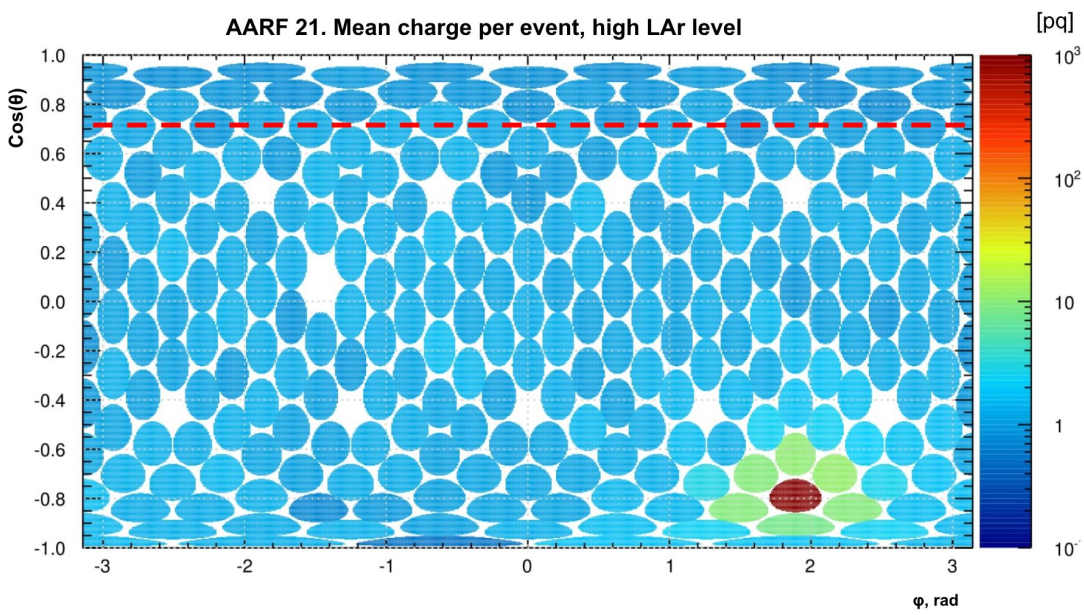

Figure 3.7: Light distribution for high LAr levels (indicated with red line) with a light source at the bottom of the vessel. Red line indicates the LAr level. Statistics for 500K events

circles and a few other nearby circles around the red AARFs PMT in Figures 3.6 and 3.7).

The overall increase in the mean charge function at all PMTs after filling the chamber with

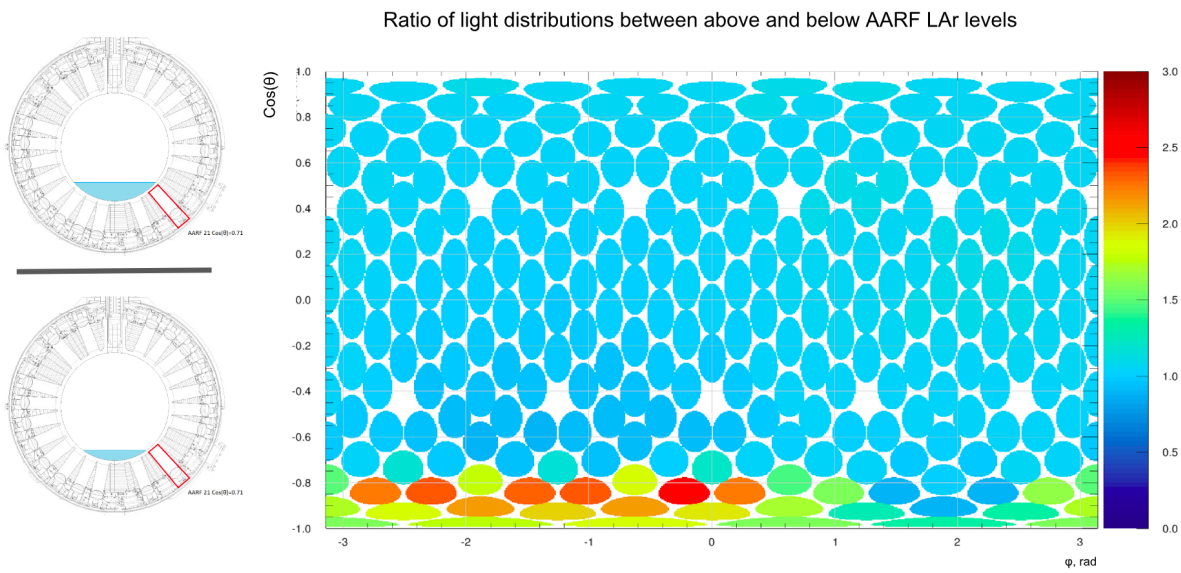

Figure 3.8: Comparison of the light distribution for low LAr level (shown with dash line) and an almost empty vessel for 500K events.

LAr is caused by random ^{39}Ar scintillation in liquid Argon. The actual background of the LAr signal is estimated looking at a time window between 2 to 1 microsecond before the pulses peak. In order to adjust each PMT to itself eliminating a PMT efficiency and gain variation, the empty tank data is taken as the reference point. The ratio of two distributions: with and without liquid argon is shown in Figures 3.8 and 3.9 for slightly filled and nearly empty detector respectively.

The **[pq]** parameter stays for the mean charge of detected photo-electrons with some particular PMT per one light injection event. Since the amount of photo-electrons is proportional to the photon number of detected light, plotting this value over all PMT's spherical coordinates in the detector (**Cos(θ)** and ϕ) gives an accurate picture how photons are distributed in the vessel.

The high intensity of incoming light into bottom PMTs in Figure 3.8 is caused by high reflection of photons from a LAr/GAr boundary. It is the same effect as in the Figure 3.9, but the flashed region is more extensive due to increasing an area of the light front through crossed distance. Another important observation from Figure3.9 is the reduction of the amount of light seen by the first neighboring PMTs around the AARF. The higher index of refraction of LAr

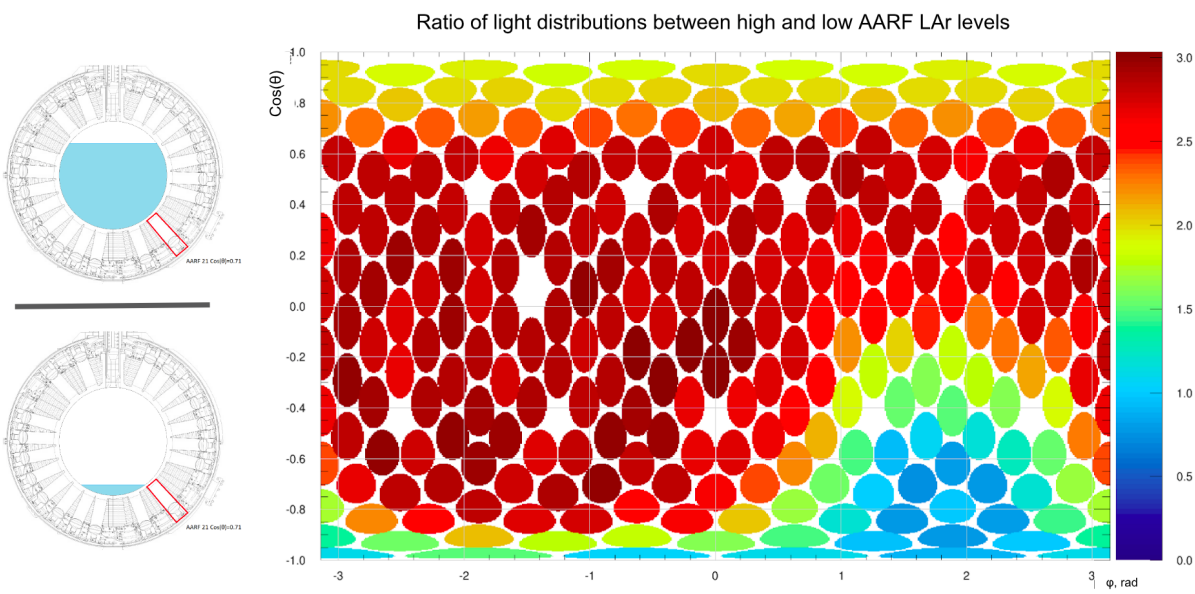

Figure 3.9: Ratio of the light yield for high LAr level (shown by a dashed line) and an almoslt empty vessel for 500K events.

compare to GAr[7] indeed reduces the reflections at the TPB optical interface. Its evidence also can be seen in Figure 3.8, where three bottom PMTs of the six first neighbors around the AARF detect less light than the upper three although an angle distribution of incoming light must have axial symmetry.

However, comparing the data with Monte-Carlo simulations, an important inconsistency in the optical model was observed. The total amount of reflected light in the simulations was greater than in the real data. Correspondingly, there is a significant difference in the number of refracted photons. It brings up the inaccuracy in TPB refractive index used in the simulations. It is also possible that TPB is so thin that the Fresnel formalism fails due to interference. for more precise correlation between the simulations and data, a complex data analysis must be provided, first attempts of which are presented in the next chapter.

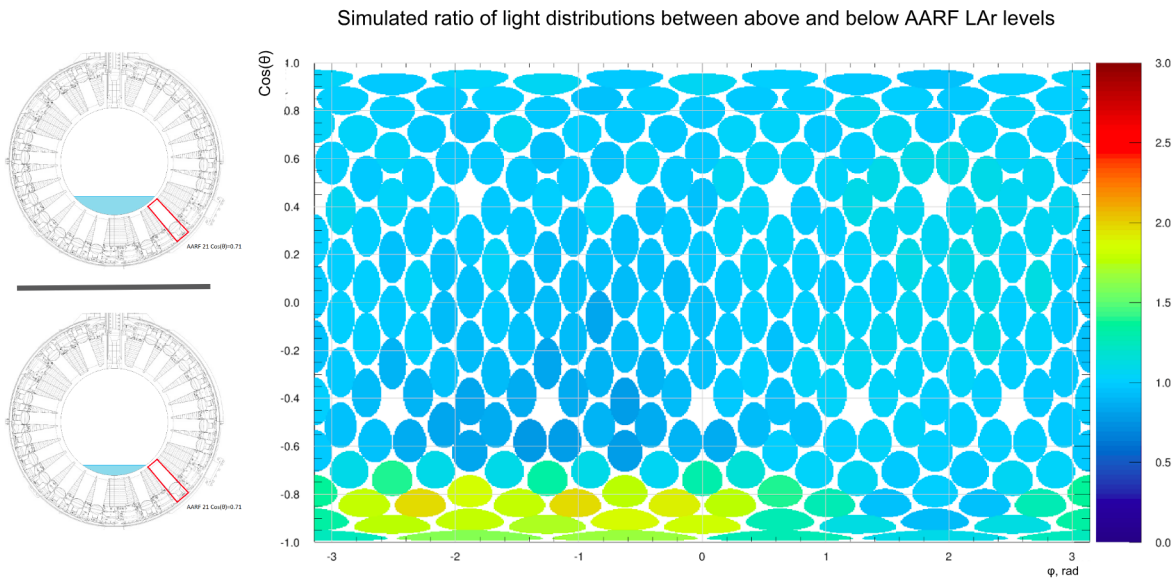

Figure 3.10: Simulation data. Ratio of the light distribution for low LAr level and an empty vessel.

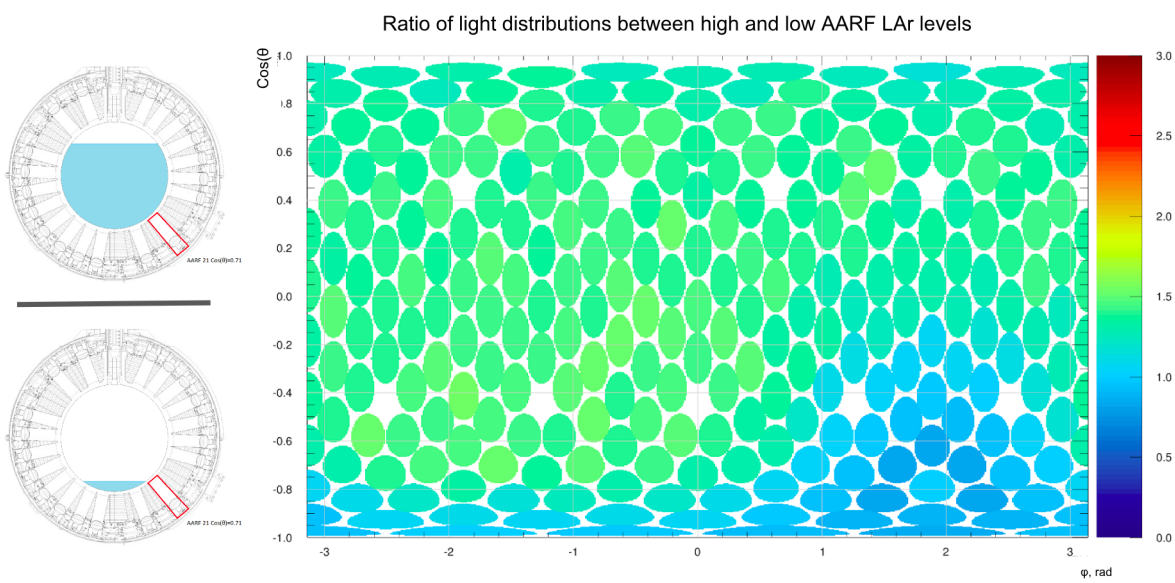

Figure 3.11: Simulation data. Ratio of the light distribution for high LAr level and an empty vessel.

3.4 TPB Optical Properties

In order to work in the spectrum of PMT quantum efficiency, a few micrometers layer of organic 1,1,4,4-tetraphenyl-1,3-butadiene (TPB) wavelength shifter was placed into the internal side of the acrylic chamber. An evaporation method allowed to distribute the material equally

over the surface. However, since evaporation can't guarantee a perfect spherical symmetry of grown crystal patterns, experimental data analysis is important for calculating the effect of TPB for optical processes in the DEAP-3600. The refractive index and typical distance between scatters are two main parameters which dictate the behavior of theoretical simulations. Monte-Carlo statistics were provided simultaneously in order to compare existing TPB parameters along with measured ones. Unfortunately, it is impossible to separate all the optical parameters for a direct measurement from each other, which makes the data analysis very complex.

The data used in this study are sets of AARF data with the same flashing condition but the following detector configurations: before the TPB deposition, after TPB deposition with vacuum in the AV and after TPB deposition with liquid Argon in the AV. In the case of perfect spherical symmetry, this would be enough for first-order results of the TPB optical properties. However, the surface roughness of both the acrylic and TPB materials does not allow for sole reliance on that data.

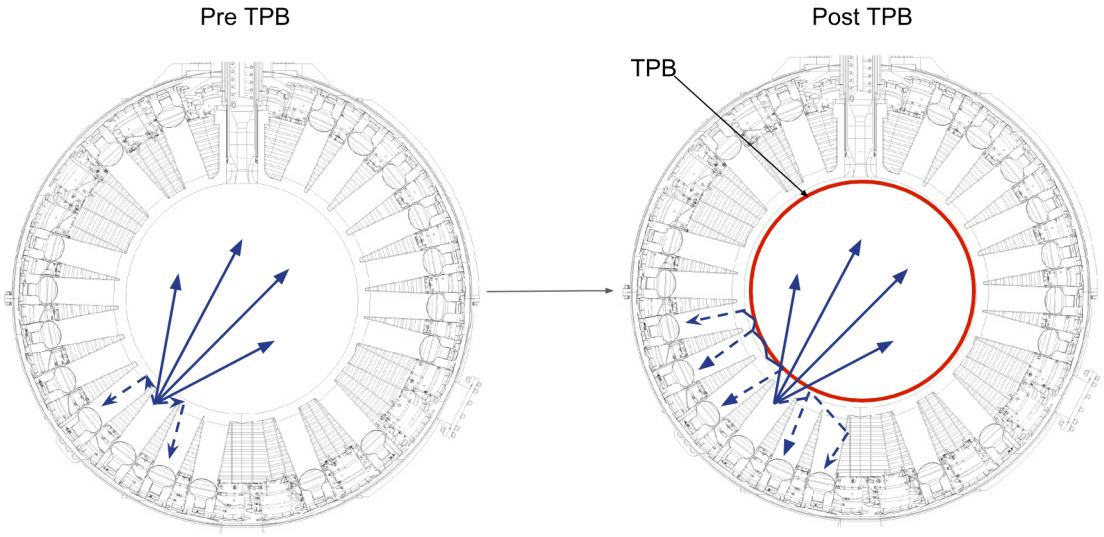

Figure 3.12: Qualitative impact of TPB presence: more photons get trapped inside acrylic light guides.

3.4.1 Changes in Light Distribution

The impact of TPB can be explained qualitatively. The additional thin layer between the acrylic and inner vessel medium (liquid argon or gaseous nitrogen) creates more boundaries of materials with different indexes of refraction. In the first case, with no TPB, photons move from a region of lower phase velocity to a higher one. As a result, a significant portion of photons get reflected and some photons may remain confined within the AV due total internal reflection until they get detected by one of the PMTs close to the AARF. Data shows that a significant fraction of photons are detected inside a 60° opening angle zone around the AARF (Figure 3.4). By replacing gaseous nitrogen or vacuum in the chamber (refractive index 1.00) with LAr (refractive index 1.23 for 400 nm wavelength [24]), this effect is diminished, which was shown in the previous section. Even though the refractive index of TPB is still under discussion, from the first data analysis results it was estimated to be 1.7 for 400 nm wavelength. Thus, even though photons can leave acrylic and transfer into a higher phase velocity zone, they may get reflected from the TPB-medium interface.

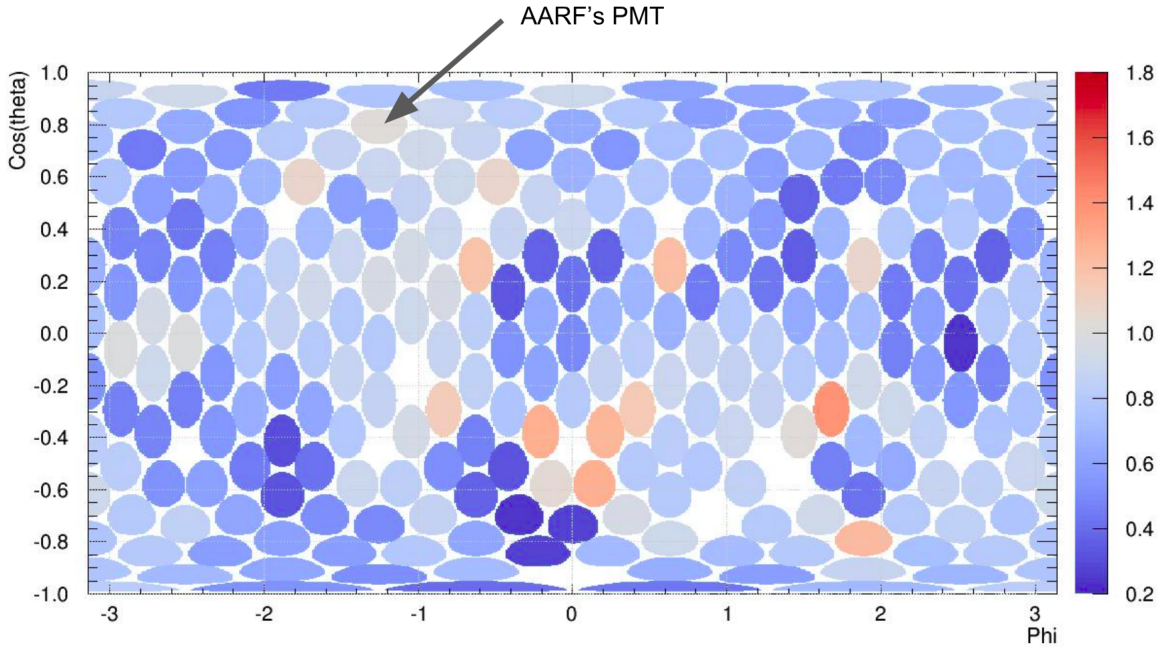

Figure 3.13: Comparison of light distributions with a light source in the AARF ID 1. Statistics for 500K events. Each slot represents the ratio of detected light after and before the TPB was installed.

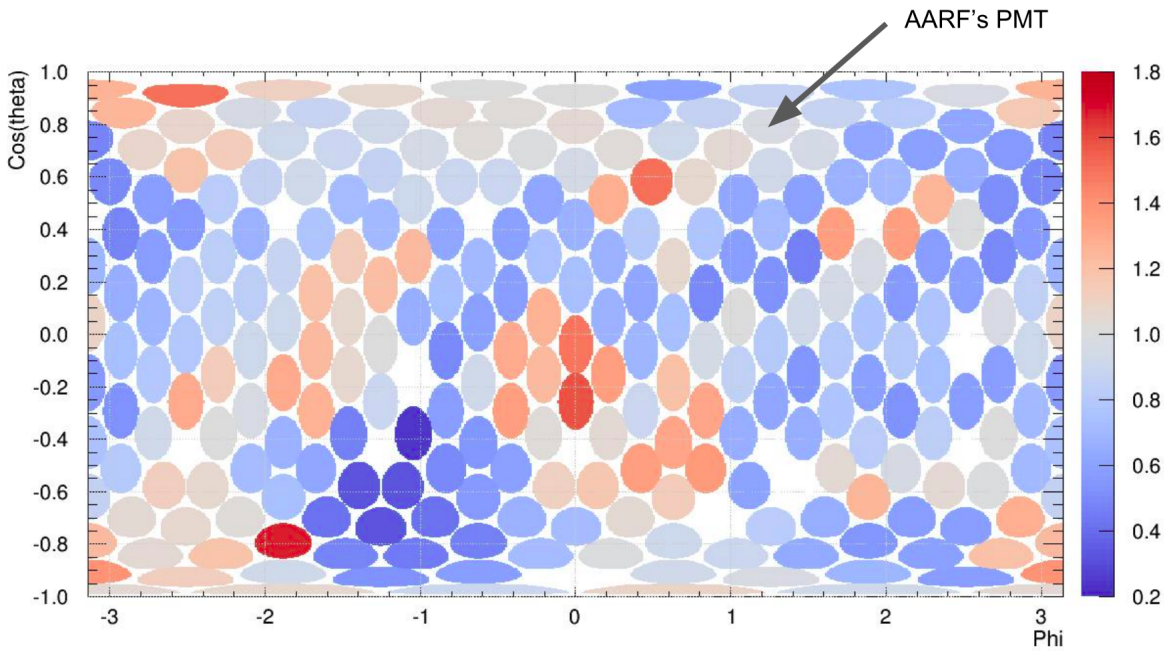

Figure 3.14: Comparison of light distributions with a light source in the AARF ID 3. Statistics for 500K events. Each slot represents the ratio of detected light after and before the TPB was installed.

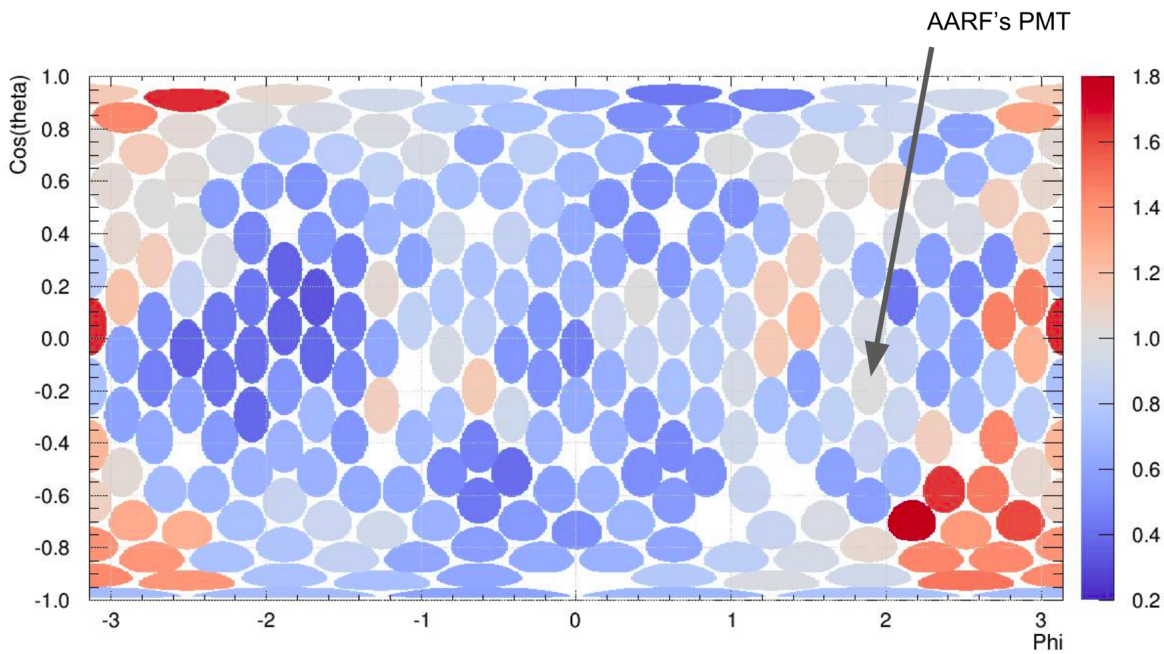

Figure 3.15: Comparison of light distributions with a light source in the AARF ID 8. Statistics for 500K events. Each slot represents the ratio of detected light after and before the TPB was installed.

In order to find the difference between photon distributions, an average number of detected photons was calculated for every PMT for two cases: before and after TPB deposition. Three different AARF locations were used to compare the consistency and symmetry of the pattern. Working with the ratio of the distributions, one can cancel out a PMT's efficiency, which differs slightly over PMTs. As predicted, the total amount of transmitted light into the vessel decreased after depositing TPB crystals. Since the power of the LED source dictates the integral of the total charge among the PMTs, it remains the same.

3.4.2 Pulse Delay

Inconsistency in charge distributions over different light sources might be caused by the roughness of the TPB layer and its scattering distance. Comparison of the shortest times, in which photons can travel between PMTs, can be a useful method for estimating TPB optical parameters. The electronics used in the DEAP-3600 allows for detection of the photon's arrival time with a precision of 1 ns driven by the PMT transit time spread. Applying the pulse-counting method pulse-time distribution can be recorded for every PMT. Then, fitting the front part of the distribution with a Gaussian distribution, the shortest time was estimated at the half-maximum point. The sample of all the pulse distributions by PMT ID is shown in Figure 3.16. The normalization was done assuming zero time difference of arriving photons to the AARF's PMT, though this method has a considerable uncertainty due to the saturation effect. Figures 3.17-3.19 show the impact of the TPB on the travelling time of photons from one of AARF's PMT, serving as the light injector.

After analyzing data for three different light sources (Figures 3.17, 3.18, 3.19), the first conclusion drawn is that photons not in the direct vicinity or line of sight of the AARF source spend more time in the AV after TPB deposition. It does not affect the first two circles of neighbors, which detect photons reflected in acrylic. The difference for light transmitted into the chamber is significant. Not only bouncing, but also scattering affects this time as well. When transiting into the AV with a wider spectrum of angle distribution, the amount of paths

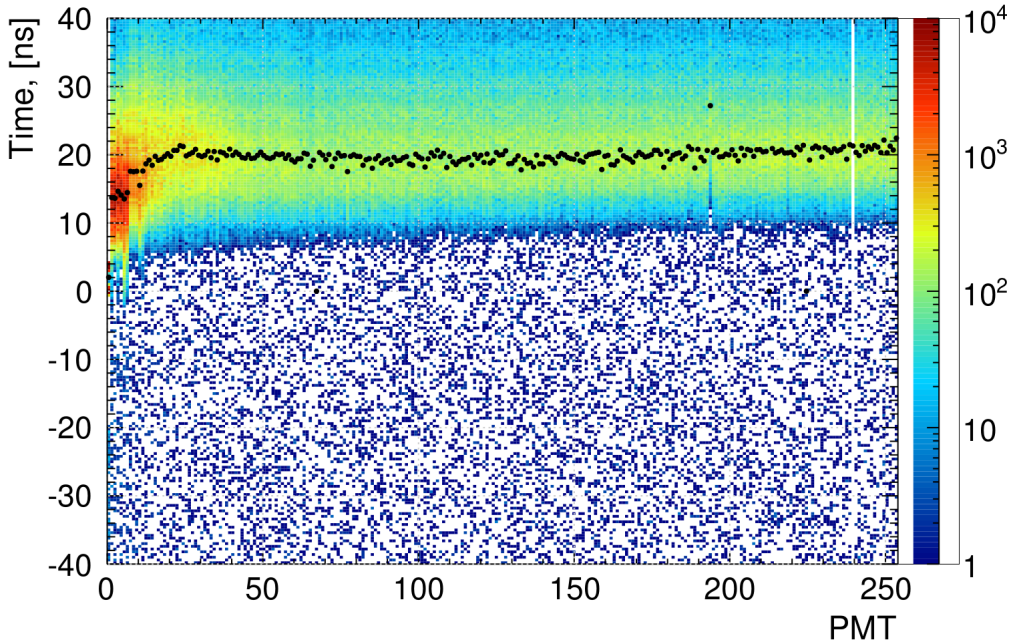

Figure 3.16: Sample of total amount of incoming pulses over time distribution. The time scale is the difference between PMT reading and trigger time. PMTs are rearranged based on the distance to the light source. Statistics for 500K events. AARF light source ID 1.

due to scattering and TPB roughness between two PMTs increases. High dependency of time fluctuations over the position of the light source proves the fact that the reflection angle of the light beam from the AARF's PMT varies significantly in different light guides. However, in some regions data is consistent for different light sources. In some zones of the longest time delays the total amount of detected photons decreases. Unfortunately, it is still unclear whether this effect is the consequence of high dependency on the refraction angle over the TPB surface or the evidence of more complex effects such as thin film interference.

Based on the charge and time analysis, together with the use of Monte-Carlo simulation methods, the TPB refractive index was estimated as 1.7 for a 400 nm wavelength, which is consistent with Reference [7]. However, studying the optical parameters of the TPB for a VUV spectrum is still in the active phase. Meanwhile, the main optical parameters estimated for the DEAP-3600 are listed in Table 3.1.

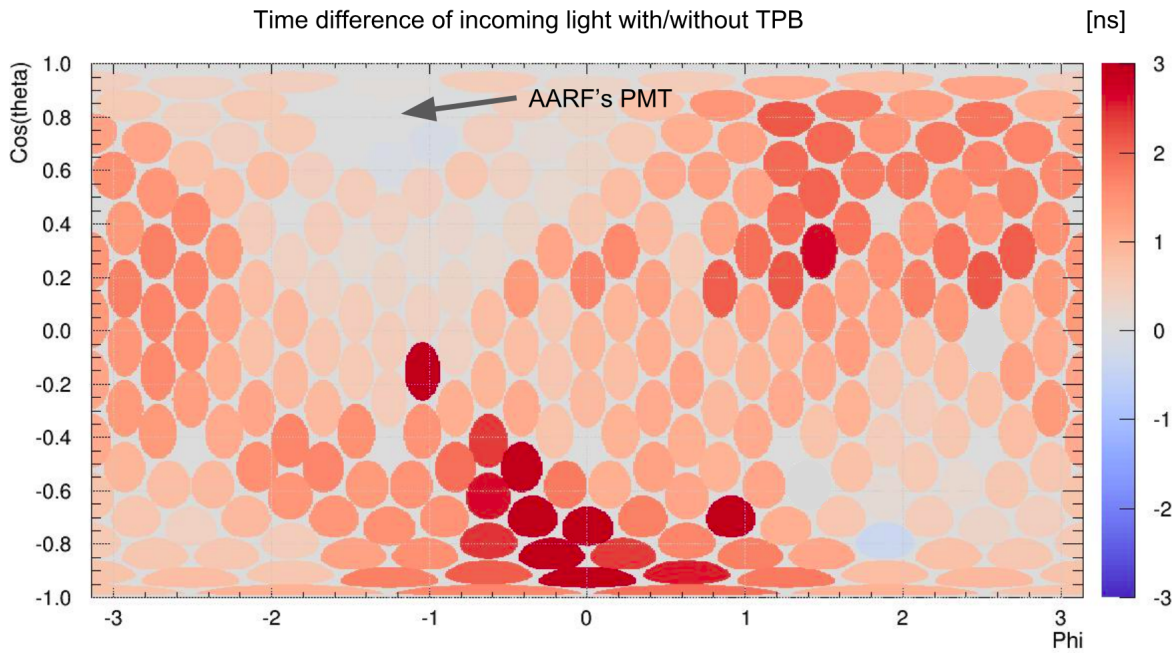

Figure 3.17: Average time delay for first incoming photons after implementing TPB over all PMTs. Statistics for 500K events. AARF light source ID 1.

Parameter	Estimated value
LAr index of refraction	1.25
LAr scattering length	∼10 [m]
TPB average thickness	3 +/- 0.02 [um]
TPB index of refraction	∼1.7
TPB scattering length	3 [um]

Table 3.1: Current estimation of main optical parameters for the DEAP-3600 inner detector

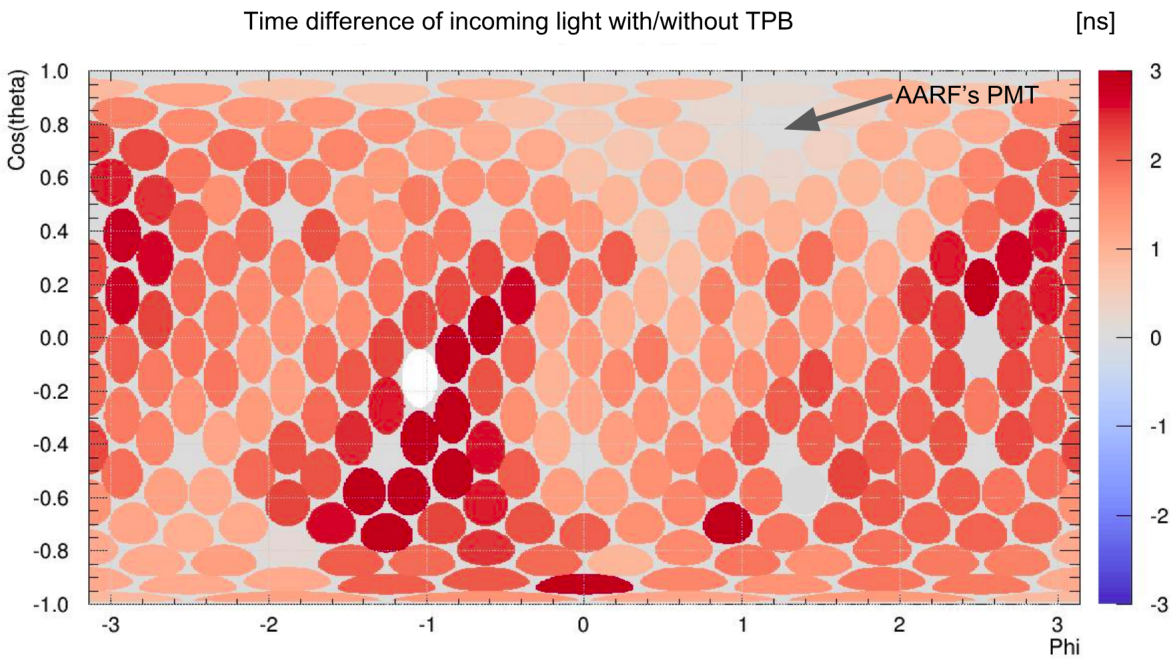

Figure 3.18: Average time delay for first incoming photons after implementing TPB over all PMTs. Statistics for 500K events. AARF light source ID 3.

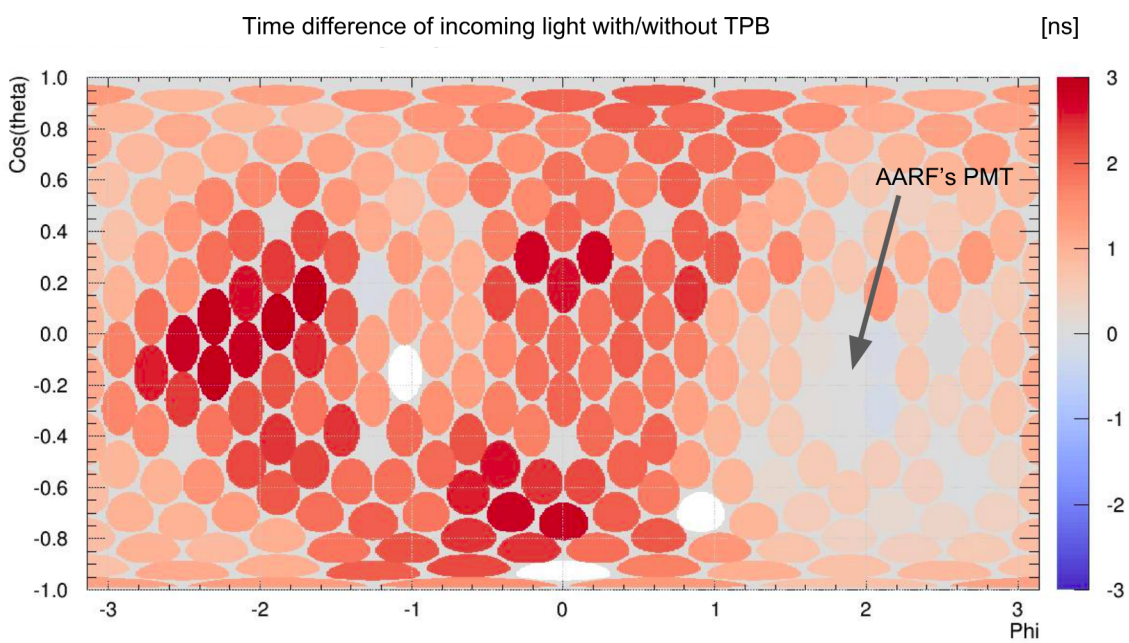

Figure 3.19: Average time delay for first incoming photons after implementing TPB over all PMTs. Statistics for 500K events. AARF light source ID 8.

Chapter 4

Summary

The main result of this work is a summary and a qualitative description of the DEAP-3600 optical calibration, along with the first attempts of estimating some physical values of used materials in the inner detector. The results shown in the section 3.3 emphasize an inaccuracy of current estimations of TPB optical parameters, such as index of refraction. However, the data justified the assumption of a glassy LAr/GAr boundary model, used in the Monte-Carlo simulations. The data also demonstrated a presence of a much higher scattering rate in TPB than was predicted. Comparison of different LED sources proved an inconsistency in angular distributions of incoming light. The detailed study of the TPB optical parameters is still in the active phase. This work showed the estimation of its index of refraction to be greater than 1.5. More accurate estimation of this number requires a complex data analysis and deep usage of the Monte-Carlo simulations.

Bibliography

[1] Peter AR Ade, N Aghanim, M Arnaud, M Ashdown, J Aumont, C Baccigalupi, AJ Banday, RB Barreiro, JG Bartlett, N Bartolo, et al. Planck 2015 results-xiii. cosmological parameters. *Astronomy & Astrophysics*, 594:A13, 2016.

[2] P. A. Amaudruz, M. Baldwin, M. Batygov, B. Beltran, C. E. Bina, D. Bishop, J. Bonatt, G. Boorman, et al. First Results from the DEAP-3600 Dark Matter Search with Argon at SNOLAB. *Physical Review Letters*, 2018.

[3] P.-A. Amaudruz, M. Baldwin, M. Batygov, B. Beltran, C.E. Bina, D. Bishop, J. Bonatt, G. Boorman, M.G. Boulay, B. Broerman, et al. Design and construction of the DEAP-3600 dark matter detector. *Astroparticle Physics*, 108:1–23, 3 2019.

[4] P-A Amaudruz, M Batygov, B Beltran, CE Bina, D Bishop, J Bonatt, G Boorman, Mark Guy Boulay, B Broerman, T Bromwich, et al. In-situ characterization of the hamamatsu r5912-hqe photomultiplier tubes used in the deap-3600 experiment. *Nuclear Instruments and Methods in Physics Research Section A: Accelerators, Spectrometers, Detectors and Associated Equipment*, 922:373–384, 2019.

[5] P-A Amaudruz, M Batygov, B Beltran, J Bonatt, K Boudjemline, Mark Guy Boulay, B Broerman, JF Bueno, A Butcher, B Cai, et al. Measurement of the scintillation time spectra and pulse-shape discrimination of low-energy β and nuclear recoils in liquid argon with deap-1. *Astroparticle Physics*, 85:1–23, 2016.

[6] Claude Amsler, V Boccone, A Büchler, R Chandrasekharan, C Regenfus, and J Rochet. Luminescence quenching of the triplet excimer state by air traces in gaseous argon. *Journal of Instrumentation*, 3(02):P02001, 2008.

[7] Ashu-Kumar Bansal and Alfons Penzkofer. Spectroscopic and travelling-wave lasing characterisation of tetraphenylbenzidine and di-naphtalenyl-diphenylbenzidine. *Applied Physics B*, 91(3-4):559–569, 2008.

[8] Vitalia Evgenievna Baranova, Pavel Fedorovich Baranov, Sergey V Muravyov, and Sergey V Uchaykin. Fluxgate magnetometer for measuring ultra low magnetic induction. In *Measurement in Research and Industry: Proceedings of XXI IMEKO World Congress*, pages 1–4, 2015.

[9] P Benetti, F Calaprice, E Calligarich, M Cambiaghi, F Carbonara, F Cavanna, AG Cocco, F Di Pompeo, N Ferrari, G Fiorillo, et al. Measurement of the specific activity of 39ar in natural argon. *Nuclear Instruments and Methods in Physics Research Section A: Accelerators, Spectrometers, Detectors and Associated Equipment*, 574(1):83–88, 2007.

[10] George R Blumenthal, SM Faber, Joel R Primack, and Martin J Rees. Formation of galaxies and large-scale structure with cold dark matter. *Nature*, 311(5986):517, 1984.

[11] Roelof Bottema and Jeroen PE Gerritsen. An investigation of the structure and kinematics of the spiral galaxy ngc 6503. *Monthly Notices of the Royal Astronomical Society*, 290(4):585–597, 1997.

[12] M G Boulay and the Deap Collaboration. DEAP-3600 Dark Matter Search at SNOLAB. *Journal of Physics: Conference Series*, 375(1):12027, 2012.

[13] Mark G Boulay and A Hime. Direct wimp detection using scintillation time discrimination in liquid argon. *arXiv preprint astro-ph/0411358*, 2004.

[14] B Broerman, Mark Guy Boulay, B Cai, D Cranshaw, K Dering, S Florian, R Gagnon, P Giampa, C Gilmour, C Hearns, et al. Application of the tpb wavelength shifter

to the deap-3600 spherical acrylic vessel inner surface. *Journal of Instrumentation*, 12(04):P04017, 2017.

[15] Ori Cheshnovsky, Baruch Raz, and Joshua Jortner. Emission spectra of deep impurity states in solid and liquid rare gas alloys. *The Journal of Chemical Physics*, 57(11):4628–4632, 1972.

[16] Douglas Clowe, Marua Bradač, Anthony H. Gonzalez, Maxim Markevitch, Scott W. Randall, Christine Jones, and Dennis Zaritsky. A Direct Empirical Proof of the Existence of Dark Matter. *The Astrophysical Journal*, 648(2):L109–L113, 9 2006.

[17] Planck Collaboration, P. A. R. Ade, N. Aghanim, M. Arnaud, M. Ashdown, J. Aumont, C. Baccigalupi, et al. Planck 2015 results. XIII. Cosmological parameters. 2 2015.

[18] Jan Conrad. Indirect Detection of WIMP Dark Matter: a compact review. 11 2014.

[19] P Cushman, C Galbiati, DN McKinsey, H Robertson, TMP Tait, D Bauer, A Borgland, B Cabrera, F Calaprice, J Cooley, et al. Snowmass cf1 summary: Wimp dark matter direct detection. *arXiv preprint arXiv:1310.8327*, 2013.

[20] F Duncan, AJ Noble, and D Sinclair. The construction and anticipated science of snolab. *Annual Review of Nuclear and Particle Science*, 60:163–180, 2010.

[21] Richard J Gaitskell. Direct detection of dark matter. *Annu. Rev. Nucl. Part. Sci.*, 54:315–359, 2004.

[22] P Gorel. Search for dark matter with liquid argon and pulse shape discrimination: Results from deap-1 and status of deap-3600. *arXiv preprint arXiv:1406.0462*, 2014.

[23] Emily Grace, Alistair Butcher, Jocelyn Monroe, and James A Nikkel. Index of refraction, rayleigh scattering length, and sellmeier coefficients in solid and liquid argon and xenon. *Nuclear Instruments and Methods in Physics Research Section A: Accelerators, Spectrometers, Detectors and Associated Equipment*, 867:204–208, 2017.

[24] Emily Grace, Alistair Butcher, Jocelyn Monroe, and James A Nikkel. Index of refraction, rayleigh scattering length, and sellmeier coefficients in solid and liquid argon and xenon. *Nuclear Instruments and Methods in Physics Research Section A: Accelerators, Spectrometers, Detectors and Associated Equipment*, 867:204–208, 2017.

[25] Kim Griest. The Search for the Dark Matter: WIMPs and MACHOs. *Annals of the New York Academy of Sciences*, 688(1):390–407, 6 1993.

[26] Hamamatsu. Photomultiplier Tubes Basics and Applications THIRD EDITION (Edition 3a). Technical report, 2007.

[27] T Heindl, T Dandl, M Hofmann, R Krücken, L Oberauer, W Potzel, J Wieser, and A Ulrich. The scintillation of liquid argon. *EPL (Europhysics Letters)*, 91(6):62002, 2010.

[28] Richard J. Hill and Mikhail P. Solon. WIMP-nucleon scattering with heavy WIMP effective theory. 9 2013.

[29] Karl Hille. Hubble Finds an Einstein Ring. 2018.

[30] Akira Hitachi, Tan Takahashi, Nobutaka Funayama, Kimiaki Masuda, Jun Kikuchi, and Tadayoshi Doke. Effect of ionization density on the time dependence of luminescence from liquid argon and xenon. *Physical Review B*, 27(9):5279, 1983.

[31] Bradley J Kavanagh and Anne M Green. Improved determination of the wimp mass from direct detection data. *Physical Review D*, 86(6):065027, 2012.

[32] JD Lewin and PF Smith. Review of mathematics, numerical factors, and corrections for dark matter experiments based on elastic nuclear recoil. *Astroparticle Physics*, 6(1):87–112, 1996.

[33] JG Mitchell. The argon-40argon-39 method for potassium-argon age determination. *Geochimica et Cosmochimica Acta*, 32(7):781–790, 1968.

[34] Kenzo Nakamura. Hyper-kamiokandea next generation water cherenkov detector. *International Journal of Modern Physics A*, 18(22):4053–4063, 2003.

[35] A Neumeier, M Hofmann, L Oberauer, W Potzel, S Schönert, T Dandl, T Heindl, A Ulrich, and J Wieser. Attenuation of vacuum ultraviolet light in liquid argon. *The European Physical Journal C*, 72(10):2190, 2012.

[36] Jon M Olley, Andrew Murray, and Richard G Roberts. The effects of disequilibria in the uranium and thorium decay chains on burial dose rates in fluvial sediments. *Quaternary Science Reviews*, 15(7):751–760, 1996.

[37] R. D. Peccei and Helen R. Quinn. CP Conservation in the Presence of Pseudoparticles. *Physical Review Letters*, 38(25):1440–1443, 6 1977.

[38] Chung-Lin Shan. Determining ratios of wimp-nucleon cross sections from direct dark matter detection data. *Journal of Cosmology and Astroparticle Physics*, 2011(07):005, 2011.

[39] Ian P. Stern, ADMX, and ADMX-HF ADMX-HF collaborations. Axion dark matter searches. In *AIP Conference Proceedings*, volume 1604, pages 456–461. American Institute of Physics, 2 2014.

[40] Teresa Marrodan Undagoitia and Ludwig Rauch. Dark matter direct-detection experiments. *Journal of Physics G: Nuclear and Particle Physics*, 43(1):013001, 2015.

[41] Tjeerd S van Albada, John N Bahcall, K Begeman, and R Sancisi. Distribution of dark matter in the spiral galaxy ngc 3198. *The Astrophysical Journal*, 295:305–313, 1985.

[42] Steven Weinberg. A New Light Boson? *Physical Review Letters*, 40(4):223–226, 1 1978.